MNRAS **000**, 000–000 (0000) Preprint 16 October 2018 Compiled using MNRAS LATEX style file v3.0

Thermodynamic properties, multiphase gas and AGN feedback in a large sample of giant ellipticals

K. Lakhchaura[1,2⋆], N. Werner[1,3,4], M. Sun[5], R. E. A. Canning[6], M. Gaspari[7†], S. W. Allen[6], T. Connor[8], M. Donahue[9], C. Sarazin[10]

[1] *MTA-Eötvös University Lendület Hot Universe Research Group, Pázmány Péter sétány 1/A, Budapest, 1117, Hungary*
[2] *MTA-ELTE Astrophysics Research Group, Pázmány Péter sétány 1/A, Budapest, 1117, Hungary*
[3] *Department of Theoretical Physics and Astrophysics, Faculty of Science, Masaryk University, Kotlářská 2, Brno, 611 37, Czech Republic*
[4] *School of Science, Hiroshima University, 1-3-1 Kagamiyama, Higashi-Hiroshima 739-8526, Japan*
[5] *Department of Physics, University of Alabama in Huntsville, Huntsville, AL 35899, USA*
[6] *Kavli Institute for Particle Astrophysics and Cosmology, Stanford University, 452 Lomita Mall, Stanford, CA 94305-4085, USA*
[7] *Department of Astrophysical Sciences, Princeton University, 4 Ivy Lane, Princeton, NJ 08544-1001, USA*
[8] *The Observatories of the Carnegie Institution for Science, 813 Santa Barbara Street, Pasadena, CA 91101, USA*
[9] *Physics & Astronomy Department, Michigan State University, East Lansing, MI 48824-2320, USA*
[10] *Department of Astronomy, University of Virginia, 530 McCormick Rd., Charlottesville, VA 22904, USA*

16 October 2018

ABSTRACT

We present a study of the thermal structure of the hot X-ray emitting atmospheres for a sample of 49 nearby X-ray and optically bright elliptical galaxies using *Chandra* X-ray data. We focus on the connection between the properties of the hot X-ray emitting gas and the cooler Hα+[NII] emitting phase, and the possible role of the latter in the AGN (Active Galactic Nuclei) feedback cycle. We do not find evident correlations between the Hα+[NII] emission and global properties such as X-ray luminosity, mass of hot gas, and gas mass fraction. We find that the presence of Hα+[NII] emission is more likely in systems with higher densities, lower entropies, shorter cooling times, shallower entropy profiles, lower values of $\min(t_{\rm cool}/t_{\rm ff})$, and disturbed X-ray morphologies (linked to turbulent motions). However, we see no clear separations in the observables obtained for galaxies with and without optical emission line nebulae. The AGN jet powers of the galaxies with X-ray cavities show hint of a possible weak positive correlation with their Hα+[NII] luminosities. This correlation and the observed trends in the thermodynamic properties may result from chaotic cold accretion (CCA) powering AGN jets, as seen in some high-resolution hydrodynamic simulations.

Key words: galaxies: evolution – galaxies: formation – galaxies: active – X-rays: galaxies

1 INTRODUCTION

Until the 1980s, elliptical galaxies were thought to be gasless dormant systems containing mostly old stars, a picture that was drastically changed with the advent of sensitive instruments in the X-ray, infrared and mm-bands. Many elliptical galaxies are now known to host a complex multiphase interstellar medium, ranging from the cold $\lesssim$30 K molecular clouds traced by sub-mm CO lines (e.g., Edge 2001; Edge & Frayer 2003; Salomé & Combes 2003; McDonald et al. 2012; Temi et al. 2018); the cool ∼100 K gas detected through the FIR cooling lines of [CII], [NII] and [OI] (e.g., Edge et al. 2010; Mittal et al. 2011, 2012; Werner et al. 2013); the warm ∼1000 K H_2 molecular gas seen in the NIR (e.g., Jaffe & Bremer 1997; Falcke et al. 1998; Donahue et al. 2000; Edge et al. 2002; Hatch et al. 2005; Jaffe et al. 2005; Johnstone et al. 2007; Oonk et al. 2010; Lim et al. 2012); the ionised ∼10000 K nebulae seen in the optical Hα+[NII] emission (e.g., Cowie et al. 1983; Johnstone et al. 1987; Heckman et al. 1989; Donahue et al. 1992; Crawford et al. 1999; McDonald et al. 2010); the moderately hot ∼100000 K gas detected in the FUV (e.g., Sparks et al. 2012); and the very hot $\sim10^7$ K X-ray gas.

⋆ lakhchaura.k@gmail.com
† *Einstein* and *Spitzer* Fellow

The role of the cool gas in feeding the active galactic nuclei (AGN) in these systems has remained an open question. The correlation between the jet powers, calculated from the radio-filled X-ray cavities, and the Bondi accretion rate of hot gas found by Allen et al. (2006) initially suggested ongoing hot accretion in giant ellipticals although Russell et al. (2013) later on did not find a clear correlation in a larger sample.

Using high-resolution 3D hydrodynamic simulations of massive galaxies, Gaspari et al. (2013, 2015, 2018) found that 'chaotic cold (gas) accretion' (CCA) plays an important role in the evolution of the central supermassive black hole (SMBH) and the host galaxy; this view has also been supported in other similar studies (e.g., Prasad et al. 2015). However, the exact nature of the material feeding and powering the AGN is still a subject of debate.

The cool gas in giant ellipticals has most likely an internal origin and formed through the radiative cooling of the hot X-ray emitting gas and through stellar mass loss. Werner et al. (2014) analysed a sample of ten optically and X-ray bright giant ellipticals, and found that the galaxies with extended cool gas nebulae have significantly lower entropies than the galaxies without cool gas, with a clear separation in the entropy profiles of the two groups. This indicates that the cool gas resulted from the radiative cooling of the hot phase. The cool gas develops through the formation of cooling instabilities from the hot gas, and feeds the central AGN; the radio mode feedback from the central AGN then heats the surrounding hot medium preventing it from cooling catastrophically, thus completing what is known as the 'AGN feedback cycle' (see Fabian 2012; McNamara & Nulsen 2012; Soker 2016, for reviews).

This scenario would lead to a correlation between the properties of the hot and cool phases. The ratio $t_{\rm cool}/t_{\rm ff}$, where $t_{\rm cool}$ is the local cooling time and $t_{\rm ff}$ is the free-fall time of a cooling blob, was found to be an important parameter for the formation of cooling instabilities (see Gaspari et al. 2012b; McCourt et al. 2012; Sharma et al. 2012). Based on hydrodynamic simulations of massive ellipticals and clusters of galaxies, it has been found that $t_{\rm cool}/t_{\rm ff} \lesssim 10$ is the critical condition for the cooling instabilities to form in the cores of these systems. This result was also found to be supported observationally (see Cavagnolo et al. 2009; Lakhchaura et al. 2016), although recently there have been some disagreements on the robustness of the cooling instability threshold (e.g., Hogan et al. 2017; Pulido et al. 2018; Babyk et al. 2018a).

McNamara et al. (2016) and Voit et al. (2017) found that the formation of cooling instabilities is also promoted by the adiabatic uplift of the hot gas by rising AGN jet inflated bubbles. Based on results obtained from both hydrodynamic simulations and observations, Gaspari et al. (2018) found that condensations are also promoted by subsonic turbulence and suggested the criterion $t_{\rm cool}/t_{\rm eddy} \approx 1$, where $t_{\rm eddy}$ is the turbulent eddy time, to be the best tracer of multiphase gas. Thus, in addition to entropy profiles and the $t_{\rm cool}/t_{\rm ff}$ ratio, gas motions should also be investigated in order to understand the formation of cooling instabilities in massive halos.

An alternative explanation for the presence/absence of multiphase gas in giant elliptical galaxies was given by Voit et al. (2015). Based on the results obtained for the small sample of Werner et al. (2014), Voit et al. (2015) found that all but one (NGC 4261) of the five single phase galaxies in the sample were found to have $t_{\rm cool}/t_{\rm ff} \gtrsim 20$ while all five multiphase galaxies had $5 < t_{\rm cool}/t_{\rm ff} \lesssim 20$, in the 1–10 kpc radial range. They suggest that the single-phase and multi-phase ellipticals are two intrinsically different categories of massive ellipticals. While in the single-phase ellipticals, the feedback from supernova explosions prevents the stellar ejecta from forming stars by sweeping it out of the galaxy, in multiphase ellipticals, supernova feedback is not sufficient and there the central AGN feedback maintains $t_{\rm cool}/t_{\rm ff} \approx 10$. Although the study was based on a small sample of galaxies, similar results were also obtained in the hydrodynamic simulations of Wang et al. (2018).

So far, most of the studies related to the non-gravitational processes (gas cooling/heating and AGN feedback) have focused on bright massive clusters of galaxies. However, to understand the details of these processes better, it is crucial to also study the giant elliptical galaxies, where we can resolve the central regions (where most of the non-gravitational processes take place) in a greater detail than in clusters.

In this work, we have analysed the X-ray and Hα+[NII] observations of a sample of 49 nearby X-ray and optically bright elliptical galaxies, in order to understand the cool-hot gas connection, their interplay and their role in the AGN feedback cycle. About 19 of the 49 galaxies are the central galaxies of their respective groups; four are central galaxies of clusters; 23 are non-central galaxies of groups/clusters and 3 are isolated/fossil galaxies. Our sample has a high degree of completeness above certain X-ray and optical luminosity thresholds (see §2.1). The sample selection is described in §2.1, and the data reduction and analysis are detailed in §2.2. The results are presented in §3, discussed in §4, and the conclusions are summarised in §5. A lambda cold dark matter cosmology with $H_0 = 70$ km s^{-1} Mpc^{-1} and $\Omega_{\rm M} = 0.3$ ($\Omega_\Lambda = 0.7$) has been assumed throughout.

2 SAMPLE AND DATA

2.1 Sample Selection

We started with the parent sample of Dunn et al. (2010) and selected 52 galaxies within 100 Mpc for which archival *Chandra* X-ray observations were available. We also included an additional 16 X-ray and optically bright galaxies which were missing from the original selection (e.g., NGC5813). To make our sample represent the actual population of nearby bright ellipticals, we selected our final sample based on the intrinsic properties of the galaxies (the X-ray luminosity of the hot gas and the absolute visible band magnitude).

The 0.5–7.0 keV X-ray luminosities at $r < 10$ kpc for all the galaxies (see §2.2 and §3.1) are given in Table 1. We obtained the visible band magnitudes for the entire sample from the NASA/IPAC Extragalactic Database (NED; Mazzarella et al. 2001), which were then converted to absolute magnitudes (B_T) based on the mean redshift-independent distances given in NED (see Table 1). We applied a lower limit of 10^{40} erg/s to the 0.5–7.0 keV X-ray halo luminosity and an upper limit of -20 to B_T. These selection criteria led to a sample size of 54. Due to short exposure times,

Table 1. The names, redshifts (z), mean redshift-independent distances (D) (from NED; Mazzarella et al. 2001), positions (RA, Dec), X-ray temperatures and 0.5–7.0 keV intrinsic X-ray luminosities estimated from a 10 kpc radius circular region around the X-ray peak (see §3.1), 2–10 keV intrinsic luminosities of the central point sources and their ratio with the Eddington luminosities (see §2.2.2), morphologies and luminosities of the Hα+[NII] emission, the 1.4 GHz flux densities and absolute visible band magnitudes (B_T) of the galaxies. The Hα+[NII] morphology/extent classification (column 10) is as follows: N: no cool gas emission, NE: Hα+[NII] extent < 2 kpc, E: Hα+[NII] extent ≥ 2 kpc and U: galaxies for which the presence/absence of Hα+[NII] could not be confirmed. References for columns 8, 10 ,11, 12 and 13, given as superscripts, are described at the bottom.

Target Name	z	D (Mpc)	RA (J2000)	Dec (J2000)	kT (keV)	$L_{X_{Halo}}$ (0.5–7 keV) (10^{42} erg/s)	$L_{X_{AGN}}$ (2–10 keV) (10^{41} erg/s)	(10^{-7} L_{Edd})	Hα+[NII] morph.	$L_{H\alpha+[NII]}$ (10^{40} erg/s)	$S_{1.4}$ (Jy)	B_T Magnitude
3C 449	0.01711	72.5*	22 31 20.63	39 21 29.81	1.01±0.03	0.11±0.01	-	-	U	-	3.674 ± 0.123^{27}	-20.24 ± 0.14^{23}
IC 1860	0.0229	95.75	02 49 33.88	-31 11 21.94	1.03±0.01	0.68±0.05	-	-	$NE^{1,2}$	-	-	-21.21 ± 0.03^{24}
IC 4296	0.0124	47.31	13 36 39.05	-33 57 57.30	0.81±0.01	0.139±0.003	0.87±0.03	7.09±0.24	$E^{1,2,3}$	0.55^{12}	18 ± 1^{28}	-21.76 ± 0.09^{24}
IC 4765	0.0150	59.52	18 47 18.15	-63 19 52.14	0.91±0.02	0.49±0.05	-	-	$NE^{1,2}$	-	0.0056^{29}	-21.54 ± 0.16^{25}
NGC 57	0.0181	77.15	00 15 30.87	17 19 42.22	0.90±0.05	0.22±0.05	-	-	$N^{1,2}$	-	0.0009 ± 0.0005^{28}	-21.77 ± 0.26^{24}
NGC 315	0.0164	56.01	00 57 48.88	30 21 08.81	0.72±0.01	0.12±0.01	3.69±0.09	46.14±1.12	$U^{1,2}$	0.26^{14}	1.8 ± 0.1^{28}	-21.54 ± 0.35^{24}
NGC 410	0.0176	66.0	01 10 58.87	33 09 07.30	0.83±0.03	0.35±0.14	-	-	$NE^{1,2}$	-	0.0058 ± 0.0005^{28}	-21.58 ± 0.22^{24}
NGC 499	0.0147	60.74	01 23 11.46	33 27 36.30	1.08±0.01	0.41±0.03	-	-	$NE^{1,2}$	-	0.0007 ± 0.0005^{28}	-21.75 ± 0.20^{24}
NGC 507	0.0164	59.83	01 23 39.95	33 15 22.22	1.04±0.01	0.23±0.02	-	-	$N^{1,2}$	-	0.062 ± 0.002^{28}	-21.68 ± 0.36^{24}
NGC 533	0.0184	61.58	01 25 31.43	01 45 33.57	0.91±0.01	0.51±0.03	-	-	$E^{1,2}$	3.24^{4}	0.029 ± 0.001^{28}	-21.54 ± 0.26^{24}
NGC 708	0.0162	64.19	01 52 46.48	36 09 06.53	1.25±0.01	0.88±0.02	-	-	$E^{1,2,5,16}$	3.40^{5}	0.067 ± 0.002^{30}	-20.74 ± 0.23^{26}
NGC 741	0.0186	64.39	01 56 20.96	05 37 43.77	0.81±0.01	0.21±0.01	-	-	$N^{1,2}$	1.22^{4}	0.94 ± 0.06^{28}	-21.84 ± 0.36^{24}
NGC 777	0.0167	58.08	02 00 14.93	31 25 45.78	0.62±0.13	0.60±0.12	-	-	$N^{1,2}$	0.03^{15}	0.007 ± 0.0005^{28}	-21.33 ± 0.24^{24}
NGC 1132	0.0232	87.9	02 52 51.82	-01 16 29.0	0.95±0.02	0.17±0.02	-	-	$N^{1,2}$	-	0.0054^{31}	-21.47 ± 0.26^{24}
NGC 1316	0.0059	19.25	03 22 41.79	-37 12 29.52	0.71±0.01	0.035±0.002	0.021±0.003	0.80±0.11	$E^{1,2,6}$	0.36^{6}	150 ± 10^{28}	-22.00 ± 0.19^{24}
NGC 1399	0.0048	17.75	03 38 29.08	-35 27 02.67	1.01±0.01	0.156±0.004	-	-	$N^{1,2,7}$	0.01^{4}	2.2 ± 0.1^{28}	-20.70 ± 0.20^{24}
NGC 1404	0.0065	19.18	03 38 51.92	-35 35 39.81	0.62±0.00	0.119±0.001	-	-	$N^{1,2}$	-	0.0039 ± 0.0006^{28}	-20.44 ± 0.24^{24}
NGC 1407	0.0060	23.27	03 40 11.90	-18 34 49.36	0.82±0.01	0.067±0.003	0.016±0.002	0.57±0.07	$N^{1,2}$	0.31^{4}	0.088 ± 0.004^{28}	-21.13 ± 0.40^{24}
NGC 1521	0.0140	50.93	04 08 18.94	-21 03 06.98	0.58±0.01	0.07±0.01	-	-	$NE^{1,2}$	0.04^{15}	0.0042 ± 0.0005^{28}	-21.14 ± 0.10^{24}
NGC 1550	0.0123	67.30	04 19 37.92	02 24 35.58	1.16±0.03	1.64±0.10	-	-	$N^{1,2}$	-	0.017 ± 0.002^{28}	-21.07 ± 0.24^{24}
NGC 1600	0.0158	45.77	04 31 39.86	-05 05 09.97	1.01±0.02	0.07±0.01	-	-	$N^{1,2}$	0.40^{10}	0.062 ± 0.003^{28}	-21.37 ± 0.14^{24}
NGC 2300	0.0064	41.45	07 32 20.49	85 42 31.90	0.66±0.02	0.10±0.01	-	-	$N^{1,2}$	-	0.0029 ± 0.0005^{28}	-20.68 ± 0.22^{24}
NGC 2305	0.0113	47.88	06 48 37.30	-64 16 24.05	0.60±0.02	0.19±0.02	-	-	$NE^{1,2}$	-	-	-20.35 ± 0.21^{24}
NGC 3091	0.0122	48.32	10 00 14.13	-19 38 11.32	0.80±0.01	0.20±0.02	-	-	$N^{1,2}$	-	0.0025 ± 0.0005^{28}	-21.29 ± 0.18^{24}
NGC 3923	0.0058	20.97	11 51 01.78	-28 48 22.36	0.81±0.05	0.037±0.001	-	-	$N^{1,2}$	-	0.0010 ± 0.0005^{28}	-20.81 ± 0.77^{24}
NGC 4073	0.0197	60.08	12 04 27.06	01 53 45.65	1.63±0.01	1.05±0.05	-	-	$N^{1,2}$	-	0.0012 ± 0.0005^{28}	-21.48 ± 0.26^{24}
NGC 4125	0.0045	21.41	12 08 06.02	65 10 26.88	0.47±0.01	0.023±0.001	0.006±0.001	0.17±0.03	$U^{1,2}$	1.84^{17}	0.025 ± 0.001^{28}	-21.00 ± 0.26^{24}
NGC 4261	0.0073	29.58	12 19 23.22	05 49 29.69	0.70±0.01	0.064±0.003	0.74±0.02	8.88±0.24	$NE^{1,2,8}$	0.05^{18}	22 ± 1^{28}	-20.95 ± 0.11^{24}
NGC 4374	0.0033	16.68	12 25 03.74	12 53 13.14	0.68±0.01	0.049±0.002	0.044±0.003	0.69±0.05	$NE^{1,2,9}$	0.43^{9}	7.0 ± 0.6^{28}	-21.02 ± 0.10^{24}
NGC 4406	0.0006	16.08	12 26 11.81	12 56 45.49	0.79±0.01	0.097±0.004	0.007±0.001	0.23±0.03	E^{10}	2.97^{4}	5.0 ± 1.5^{32}	-21.20 ± 0.11^{24}
NGC 4472	0.0032	15.82	12 28 46.80	08 00 01.48	0.94±0.00	0.158±0.001	-	-	$N^{1,2}$	0.52^{4}	0.22 ± 0.01^{28}	-21.63 ± 0.14^{24}
NGC 4486	0.0042	16.56	12 30 49.42	12 23 28.04	1.64±0.00	2.157±0.004	0.63 ± 0.14^{19}	5.40±1.20	E^{4}	3.87^{22}	210 ± 10^{28}	-21.51 ± 0.09^{24}
NGC 4552	0.0009	15.97	12 35 39.80	12 33 23.00	0.61±0.00	0.029±0.001	0.16±0.01	3.84±0.24	$N^{1,2}$	0.24^{4}	0.100 ± 0.003^{28}	-20.29 ± 0.09^{24}
NGC 4636	0.0031	15.96	12 42 49.87	02 41 16.01	0.68±0.00	0.198±0.002	-	-	$NE^{4,7}$	0.65^{21}	0.078 ± 0.003^{28}	-20.58 ± 0.20^{24}
NGC 4649	0.0034	16.55	12 43 40.01	11 33 09.40	0.86±0.00	0.106±0.002	-	-	$N^{1,2}$	0.91^{10}	0.029 ± 0.001^{28}	-21.28 ± 0.11^{24}
NGC 4696	0.0098	37.48	12 48 49.28	-41 18 39.92	1.40±0.00	2.49±0.01	-	-	E^{11}	4.67^{11}	3.98 ± 0.11^{33}	-21.66 ± 0.17^{25}
NGC 4778	0.0137	59.29*	12 53 05.6	-09 12 21	0.81±0.00	0.59±0.01	-	-	$NE^{1,2}$	0.157^{13}	0.0049 ± 0.0005^{28}	-20.39 ± 0.23^{24}
NGC 4782	0.0133	48.63	12 54 35.70	-12 34 06.92	0.72±0.03	0.05±0.01	0.048±0.007	0.48±0.07	$NE^{1,2,4}$	1.02^{4}	7.0 ± 0.6^{28}	-20.74 ± 0.31^{24}
NGC 4936	0.0103	31.36	13 04 17.09	-30 31 34.71	0.89±0.04	0.06±0.01	-	-	$E^{1,2}$	1.54^{4}	0.040 ± 0.002^{28}	-20.72 ± 0.16^{25}
NGC 5044	0.009	35.75	13 15 23.97	-16 23 08.00	0.85±0.00	1.29±0.01	0.041±0.002	1.50±0.07	$E^{1,2}$	6.0^{21}	0.035 ± 0.001^{28}	-20.94 ± 0.41^{24}
NGC 5129	0.0230	86.85	13 24 10.00	13 58 35.19	0.79±0.02	0.23±0.02	-	-	$NE^{1,2}$	-	0.0072^{31}	-21.67 ± 0.22^{24}
NGC 5419	0.0139	50.87	14 03 38.77	-33 58 42.20	1.19±0.06	0.24±0.02	0.71±0.07	4.72±0.47 -	$N^{1,2}$	1.28^{4}	0.79 ± 0.06^{28}	-21.63 ± 0.36^{24}
NGC 5813	0.0064	29.23	15 01 11.27	01 42 07.09	0.67±0.00	0.497±0.003	0.008±0.001	0.24±0.03	$E^{4,7,19}$	1.16^{21}	0.015 ± 0.001^{28}	-20.88 ± 0.24^{24}
NGC 5846	0.0057	27.13	15 06 29.25	01 36 20.29	0.66±0.00	0.29±0.01	-	-	$E^{1,2}$	2.47^{21}	0.021 ± 0.001^{28}	-21.12 ± 0.25^{24}
NGC 6407	0.0154	64.93	17 44 57.66	-60 44 23.28	0.86±0.05	0.54±0.09	-	-	$U^{1,2}$	$<0.03^{4}$	-	-21.18 ± 0.15^{25}
NGC 6861	0.0094	30.09	20 07 19.48	-48 22 12.94	0.97±0.02	0.051±0.004	0.076±0.007	0.26±0.02	$E^{1,2}$	2.15^{4}	-	-20.27 ± 0.22^{24}
NGC 6868	0.0094	32.32	20 09 54.08	-48 22 46.25	0.71±0.01	0.046±0.003	0.14±0.01	3.41±0.24	$E^{1,2}$	3.46^{4}	-	-20.89 ± 0.23^{24}
NGC 7619	0.0132	50.53	23 20 14.52	08 12 22.63	0.85±0.01	0.14±0.01	-	-	$N^{1,2}$	1.86^{4}	0.02 ± 0.001^{28}	-21.42 ± 0.23^{24}
NGC 7796	0.0113	50.06	23 58 59.81	-55 27 30.12	0.60±0.01	0.035±0.004	-	-	$N^{1,2}$	$<0.01^{4}$	-	-21.04 ± 0.22^{24}

* redshift-independent distances were not available for these sources.

References for column 8, 10, 11, 12 and 13: 1. Connor et al. (2018) (in prep.) 2. Sun et al. (2018) (in prep.) 3. Grossovà et al. (2018) (in prep.) 4. Macchetto et al. (1996) 5. Plana et al. (1998) 6. Mackie & Fabbiano (1998) 7. Werner et al. (2014) 8. Ferrarese et al. (1996) 9. Bower et al. (1997) 10. Trinchieri & di Serego Alighieri (1991) 11. Fabian et al. (2016) 12. Phillips et al. (1986) 13. Valluri & Anupama (1996) 14. Ho et al. (1997) 15. Annibali et al. (2010) 16. Blanton et al. (2004) 17. Kulkarni et al. (2014) 18. Ferrarese et al. (1996) 19. Randall et al. (2011) 20. González-Martín et al. (2009) 21. Caon et al. (2000) 22. Gavazzi et al. (2000) 23. Smith & Heckman (1989) 24. de Vaucouleurs et al. (1991) 25.Lauberts & Valentijn (1989) 26. Gavazzi & Boselli (1996) 27. Laing & Peacock (1980) 28. Brown et al. (2011) 29. Oosterloo et al. (2007) 30. Condon et al. (1998) 31. Condon et al. (2002) 32. Vollmer et al. (2004) 33. Kuehr et al. (1981)

the *Chandra* observations of four of the 54 systems provided too few counts for the temperature within 10 kpc to be determined with a sufficient accuracy, rendering them unsuitable for detailed analysis. Also, the X-ray emission from the galaxy IC310 was found to be strongly dominated by the central point source. After excluding these five systems, our final sample was reduced to 49 galaxies.

For the Hα+[NII] information presented in this work, we have mainly used the results from an analysis of the Hα+[NII] observations carried out using the SOAR optical

Imager (SOI) and Goodman High Throughput Spectrograph of the 4.1 m SOuthern Astrophysical Research (SOAR) telescope (Connor et al. 2018, in prep.), as well as the Apache Point Observatory (APO) Astrophysics Research Consortium (ARC) 3.5 m telescope (Sun et al. 2018, in prep.). Note that, the Hα+[NII] morphology information presented in this paper comes from the APO and SOAR data, while the luminosities are taken from the literature.

Significant Hα+[NII] emission was detected in about half (24/49) of the galaxies. Based on the SOAR/APO results, we classified the Hα+[NII] morphologies of our sample into 4 categories. These include no cool gas emission (N; total 20 galaxies), nuclear emission (NE: 12 galaxies with Hα+[NII] emission extent $<$ 2 kpc), extended filamentary emission (E: 13 galaxies with Hα+[NII] emission extent $\geq$ 2 kpc), and unsure (U: 4 galaxies for which presence/absence of Hα+[NII] emission could not be confirmed). The 10^{th} and 11^{th} columns of table 1 show the morphology class (based on the SOAR/APO results Connor et al. 2018; Sun et al. 2018) and the luminosities (from literature) of the Hα+[NII] emission for the sample.

The detailed discussion on the imaging and spectroscopic data from SOAR and APO will be presented in two papers (Connor et al. 2018; Sun et al. 2018). The depth of the SOAR data is comparable with the APO data, both for imaging and spectroscopy. Both telescopes have similar mirror sizes and similar optical instruments for imaging/spectroscopy. Within 9" diameter of the nucleus, the 5-σ limit reached by our data is 5×10^{-15} erg s^{-1} cm^{-2}– 2×10^{-14} erg s^{-1} cm^{-2}, depending on the continuum brightness. Since the limit is essentially an equivalent width (EW) limit, our final constraint on the emission-line luminosity is better than 5×10^{39} erg s^{-1} (see Werner et al. 2014, for comparison).

Some of the Hα+[NII] flux estimates in Table 1, are taken from Macchetto et al. (1996) and are based on narrow band Hα+[NII] images. In these observations, the stellar continuum is removed by subtracting a scaled broad R-band image from the narrow band Hα+[NII] image. The scaling factor is a critical parameter in such an analysis, and various factors (e.g., a non-uniform colour across the field) may lead to wrong stellar continuum subtraction leading to spurious detections, especially when the Hα+[NII] emission is uniform (non-filamentary). As an example, for the galaxies NGC 1399 and NGC 4472, Macchetto et al. (1996) detected significant emission with disk like morphologies, although no significant Hα+[NII] emission was detected in the SOAR images and spectra. Therefore, we caution our readers that some of the disk-like emission detected in Macchetto et al. (1996) might be an artefact, and hence the accuracy of the flux estimates is limited by that of the stellar subtraction.

2.2 X-ray Data Reduction and Analysis

2.2.1 Data Reduction

We obtained the publicly available *Chandra* observations for our sample from the High Energy Astrophysics Science Archive Research Centre (HEASARC). The observation log for all the data used in the analysis is given in Table A1. We used CIAO version 4.9 (Fruscione et al. 2006) and CALDB version 4.7.3 for the data reduction, and the X-ray spectral fitting package XSPEC version 12.9.1 (AtomDB version 3.0.7) (Arnaud 1996) for the spectral analyses. Throughout the paper, the metallicities are given with respect to the Solar abundances of Grevesse & Sauval (1998). All the data were reprocessed using the standard *chandra_repro* tool. Periods of strong background flares were filtered using the *lc_clean* script, and the threshold was set to match the blanksky background maps. Point sources were detected using the CIAO task *wavdetect* with a false-positive probability threshold of 10^{-6}, they were verified by visual inspection of the X-ray images and finally filtered (except for the central point sources, see §2.2.2) from the event files. Note that, the point source detection is prone to be affected by the quality of data and S/N ratio, especially for faint sources.

2.2.2 Central X-ray Point Sources

For the galaxies for which central point sources (coinciding with the galaxy's X-ray emission peak) were detected, a visual inspection was not sufficient for verification. For these central sources, X-ray spectra were extracted from the central regions of radius 3 pixels (1.476"). The spectra were first modeled with a *wabs*apec* model and then with a *wabs(apec+pow)* model in XSPEC; the power-law index was frozen to 1.5[1]. For some of the sources an additional absorption *zwabs* model was required with the power-law to account for the intrinsic absorption of the AGN. The sources were confirmed if the addition of the powerlaw component lead to a significant improvement in the fit. In the end, central point sources were confirmed in 16 of the 49 galaxies of our sample. Interestingly, 11 of the 16 galaxies were found in systems containing cool gas (NE and E) while only three were in systems with no detectable optical emission line nebulae (N); the remaining two galaxies were in the unsure (U) systems. Note however that based on the radio flux densities given in the literature (e.g. Brown et al. 2011; Dunn et al. 2010), practically all galaxies in our sample harbour central radio sources (except NGC 2305 for which we did not find a reported detection).

The intrinsic 2–10 keV central AGN luminosities estimated from the power-law components of the spectral models and their ratio with the Eddington luminosities are given in the eighth and ninth columns of Table 1, respectively. The Eddington luminosities were calculated using the relation $L_{\rm Edd} = 1.26\times10^{47}(M_{\rm BH}/10^9 M_\odot)$ erg/s (Russell et al. 2013). The Black Hole masses ($M_{\rm BH}$) were estimated from the empirical correlation of M_{BH}-σ_* relation (Gebhardt et al. 2000; Tremaine et al. 2002), $M_{\rm BH} = 10^{8.13}(\sigma_*/200 \text{ km s}^{-1})^{4.02}$ $M_\odot$. The velocity dispersions (σ_*) were obtained from the Hyperleda database (Makarov et al. 2014). For NGC 4486 (M87), the central source was heavily affected by pile-up, therefore the AGN luminosity of González-Martín et al. (2009) was used. All the AGNs are found to have very low Eddington ratios ($<10^{-5}$) and seem to be operating in the gentle radio mechanical feedback mode. For the remaining analyses, the central point sources for all the 16 galaxies

[1] To avoid the degeneracy between the *apec* and *pow* components, it was required to freeze the power law index. The value of 1.5 is consistent with the values typically seen for such sources (e.g. David et al. 2009)

were removed by excluding the central regions of radius 3 pixels (1.476").

2.2.3 Spectral Extraction

For this study we determined emission weighted average properties within a radius of 10 kpc as well as the deprojected radial profiles of the thermodynamic properties of the hot diffuse halos. For the average properties, we restricted the spectral analyses to $r < 10$ kpc ($\sim R_e$ for most of the galaxies, see Goulding et al. 2016) since the hot gas properties within this region are dominated by the galaxy scale physics. For this, spectra were extracted from a circular region within $r < 10$ kpc centred on the galaxy's X-ray peak, using the CIAO task *specextract*. For the radial profiles, spectra were extracted from a number of circular annuli centred on the X-ray peak. The radial ranges of the annuli were chosen based on the requirement that each annulus should have at least 100 counts in the 0.5–5 keV energy range. The total number of annuli was limited to be $\leq$25. For the radial analyses, the spectra from the outermost annuli in some of the galaxies may be contaminated by the emission from the surrounding group or cluster. However, the values obtained for these annuli do not affect our main results.

2.2.4 Background Spectra

For each source spectrum, corresponding background spectra were extracted from the standard Chandra blanksky background event files matching the source observations, obtained from Maxim Markevitch's blank-sky background database. The event files were reprojected to match the source observations. To match the time-dependent particle background levels in the source and blanksky observations, all the blanksky spectra were scaled by the ratio of the 9.5–12 keV count rates of the source and blanksky observations.

We also checked for contamination by soft Galactic foreground (most significant in the outermost annuli) and for differences in the Galactic foreground level in the scaled blanksky and source spectra. For this, we obtained the *ROSAT* All Sky Survey 0.47–1.21 keV (RASS 45 band) count rates from the outer 0.7–1.0 degree annular regions around each galaxy using the HEASOFT X-ray background tool. These count-rates were compared with the source count-rates in the outermost annuli. For most of our galaxies (39/49), the R45 count rates were <10% of the total 0.47–1.21 keV count-rates.

We chose the two worst affected sources, NGC 4552 and NGC 4778 (HCG 62), for which the RASS R45 count rate was $\gtrsim$ 20% of the total 0.47–1.21 keV count-rate. The annuli spectra for these sources were analysed with two additional model components: a 0.25 keV *APEC* component with one-third solar metallicity for the Galactic halo and a 0.3 keV *APEC* component with solar metallicity for the Local Hot Bubble; both non-deprojected. The normalizations of these components were allowed to be negative and their values for all outer annuli were tied to that of the innermost annulus with a multiplicative factor equal to the ratio of the respective areas. We found that the addition of the Galactic background components in the model for the two most affected galaxies lead to no significant changes in the final results.

2.2.5 Spectral Analysis

The spectra for the central r =10 kpc were fitted with a single-temperature absorbed *VAPEC* model in XSPEC, using the C-statistics. A thermal bremsstrahlung component with $kT = 7.3$ keV was added to account for the unresolved point sources (see Irwin et al. 2003). The neutral hydrogen column density was obtained from the *Swift* Galactic $N_{\rm H}$ tool which gives the total (atomic+molecular) X-ray absorbing Hydrogen column density, using the method of Willingale et al. (2013). The redshift was fixed to the value obtained from the SIMBAD database (Wenger et al. 2000). The abundances of Mg, Si and Fe were kept free for this analysis. However, for the galaxies for which the abundances could not be constrained, they were frozen to one-third of the solar value, which is the value obtained for most of the galaxies in the sample.

For the radial profiles, all the metallicities were frozen to the values obtained from the above analysis of the central 10 kpc radius regions. For low-temperature systems ($kT \sim$0.5–1.0 keV), this assumption might lead to an underestimation of metallicities and overestimation of densities (see Buote 2000; Werner et al. 2008), particularly in the inner regions where the gas is expected to be multiphase. However, for many of the galaxies, the data quality did not allow us to resolve the multi-temperature structure and the metallicities could not be constrained for the individual annuli. Therefore, to analyse the entire sample in a uniform way, we assumed the central 10 kpc region metallicities when fitting the radial profiles. Note that underestimating the metallicity by a factor of 2, will result in overestimating the density by a factor of $\sim$1.35[2] (Werner et al. 2012).

The deprojection analysis to determine the radial profiles of thermodynamic quantities was performed using the *projct* model in XSPEC. The free parameters in the fit were the temperature and normalization of the *APEC* component and the normalization of the bremsstrahlung component (not deprojected). We assumed a constant density and temperature in each 3D shell. The *APEC* normalizations (η) were converted to the individual shell gas densities ($n = n_e + n_i$) using the relation

$$\eta = \frac{10^{-14} \int n_e n_p dV}{4\pi {D_A}^2 (1+z)^2}. \quad (1)$$

Here D_A is the angular diameter distance to the source, n_e and n_p are the electron and proton number densities, where for a fully ionised gas with one-third solar abundance $n_e = 0.53n$ and $n_p = n_e/1.2$. The densities and temperatures were used to calculate the gas entropy ($K = kTn_e^{-2/3}$), pressure ($P = nkT$), and cooling time ($t_{\rm cool} = 1.5nkT/(n_e n_i \Lambda(T,Z))$, where $\Lambda(T,Z)$ is the cooling function and Z is the metallicity; note that we are using here the

[2] We also checked for the effect of using projected metallicity profiles (with 2T apec models for the inner shells) instead of fixed metallicities, for two (a cool gas free and a cool gas rich) galaxies with high data quality. This lead to very similar changes (<10% decrease in the densities, <20% increase in the entropy and ~8% decrease in the slopes of the entropy profiles) in both the galaxies. We think that for all our galaxies, a free metallicity will shift all the density profiles slightly upwards and the entropy and cooling times profiles downwards, however, the general trends in Figs. 2 and 3 will remain the same.

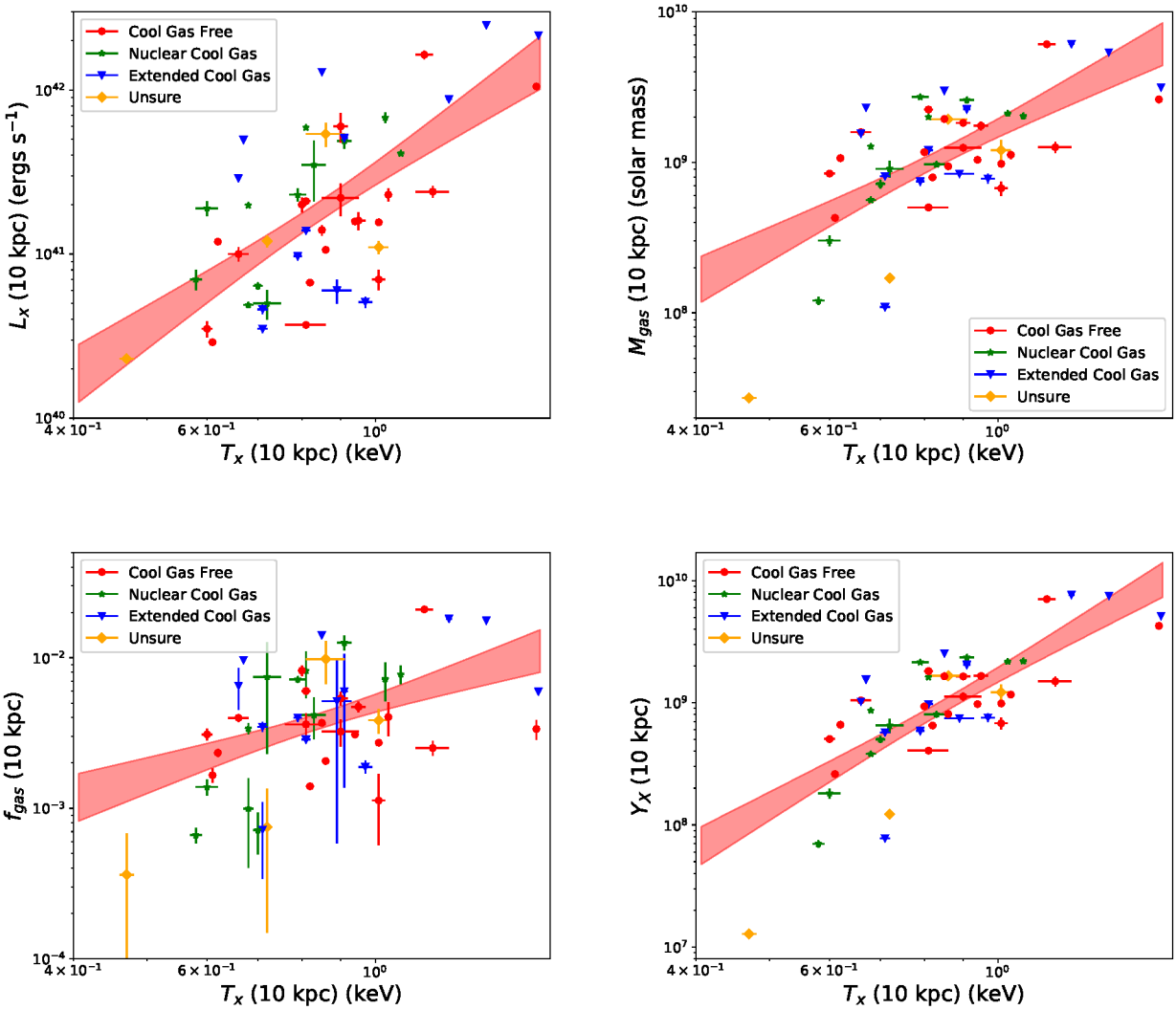

Figure 1. The 0.5–7.0 keV X-ray luminosities (upper left), the total gas masses (upper right), the gas mass fractions (lower left) and the $Y_X = M_{gas}T_X$ (lower right) values, estimated from within a radius of 10 kpc plotted as a function of the gas temperatures determined from the same region. The red, green, blue and orange colors denote the cool gas free, nuclear cool gas, extended cool gas and unsure systems, respectively. The shaded regions show the best fit relations ($Y = AX^B$) of the y-axis variables with the x-axis, see Table 2.

metallicities obtained from the central 10 kpc region spectral analysis).

3 RESULTS

3.1 X-ray Properties within r=10 kpc

The spectra for all the 49 galaxies extracted from circular regions of $r = 10$ kpc around the X-ray peaks were analyzed as described in §2.2. The resulting best-fit values of the gas temperatures span a range of values from 0.47 keV to 1.64 keV. The 0.5–7.0 keV X-ray luminosities (L_X) determined within $r = 10$ kpc span two orders of magnitude from 2.3×10^{40} erg s^{-1} to 2.5×10^{42} erg s^{-1}. The temperatures and X-ray halo luminosities obtained for the entire sample are listed in Table 1. The X-ray halo luminosities plotted vs. the average X-ray temperatures of the galaxies are shown in the top left panel of Fig. 1.

3.2 Deprojected Profiles

The deprojected temperature (kT), density (n), entropy (K), pressure (P) and cooling time (t_{cool}) profiles of the individual galaxies are given in the appendix (Figs. A.1, A.2, A.3, A.4 and A.5, respectively). The kT, n, K and cooling time (t_{cool}) profiles of the full sample, classified based on the cool gas extents (see §2.1) are shown in Fig. 2. The temperature profiles in the top left panel, do not show any distinction between the different cool gas morphology/extent groups. The density profiles show higher densities for the extended cool gas (blue) galaxies than the rest of the galaxies. However, at least 3 (NGC 4936, NGC 6868 and IC 4296) of the 13 extended cool gas galaxies seem to have low den-

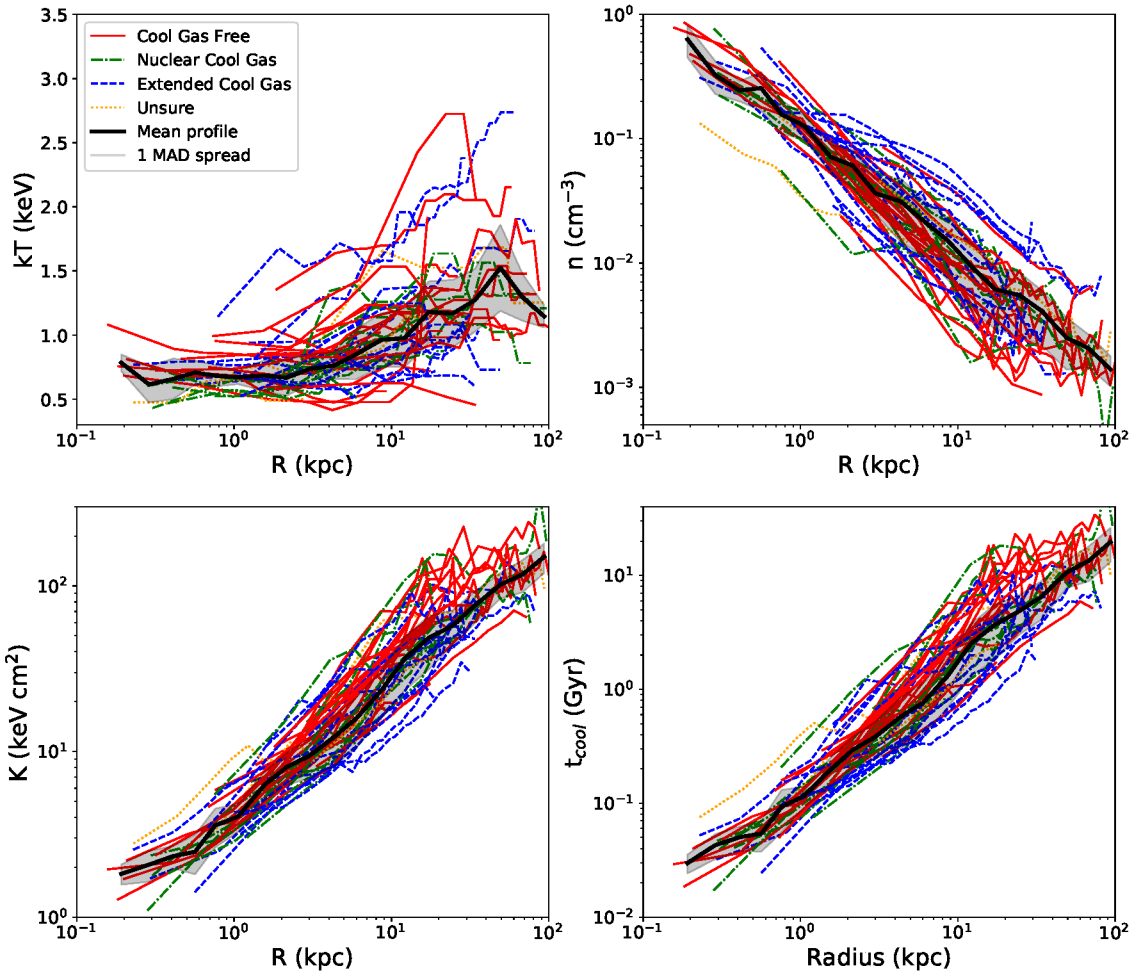

Figure 2. The profiles of temperature (top left), density (top right), entropy (bottom left) and cooling time (bottom right) for the full sample (see §3.2). The red (solid), green (dashed-dotted), blue (dashed) and orange (dotted) lines denote the cool gas free, nuclear cool gas, extended cool gas and unsure systems, respectively. The black line shows the median profile for the full sample and the grey shaded regions show the median absolute deviation (MAD) spreads about the medians.

sities. Note that, NGC 6868 was found to have indications for a rotating cold gas disk in the velocity distribution maps of [CII] emission (see Werner et al. 2014). It is possible that the cool gas in the low density galaxies is supported by rotation. In general, the profiles of entropy and cooling time show lower values for the extended cool gas galaxies than the cool gas free galaxies. The three outliers with low density and extended cool gas, also have higher entropies and cooling times than the rest of the extended cool gas galaxies.

To see the trends in the thermodynamic profiles and their scatter more clearly, in Fig. 3 we show the median temperature, density, entropy and cooling time profiles of the cool gas free (red), nuclear cool gas (green) and extended cool gas (blue) groups. The profiles were obtained by finding the median values in 15 radial bins. The shaded regions show the median absolute deviations (MAD) about the medians for each group. The trends seen in Fig. 2 are much more clearly visible in Fig. 3. The median temperature profiles of the three groups are found to be very similar. The density profiles show higher values for the extended cool gas galaxies than the cool gas free galaxies. In the entropy and cooling time profiles also, the extended cool gas galaxies seem to have lower values than the cool gas free galaxies, especially outside the innermost regions (∼2 kpc), but with significant spread. The nuclear cool gas galaxies are found to have densities, entropies and cooling times in between the extended cool gas and cool gas free galaxies.

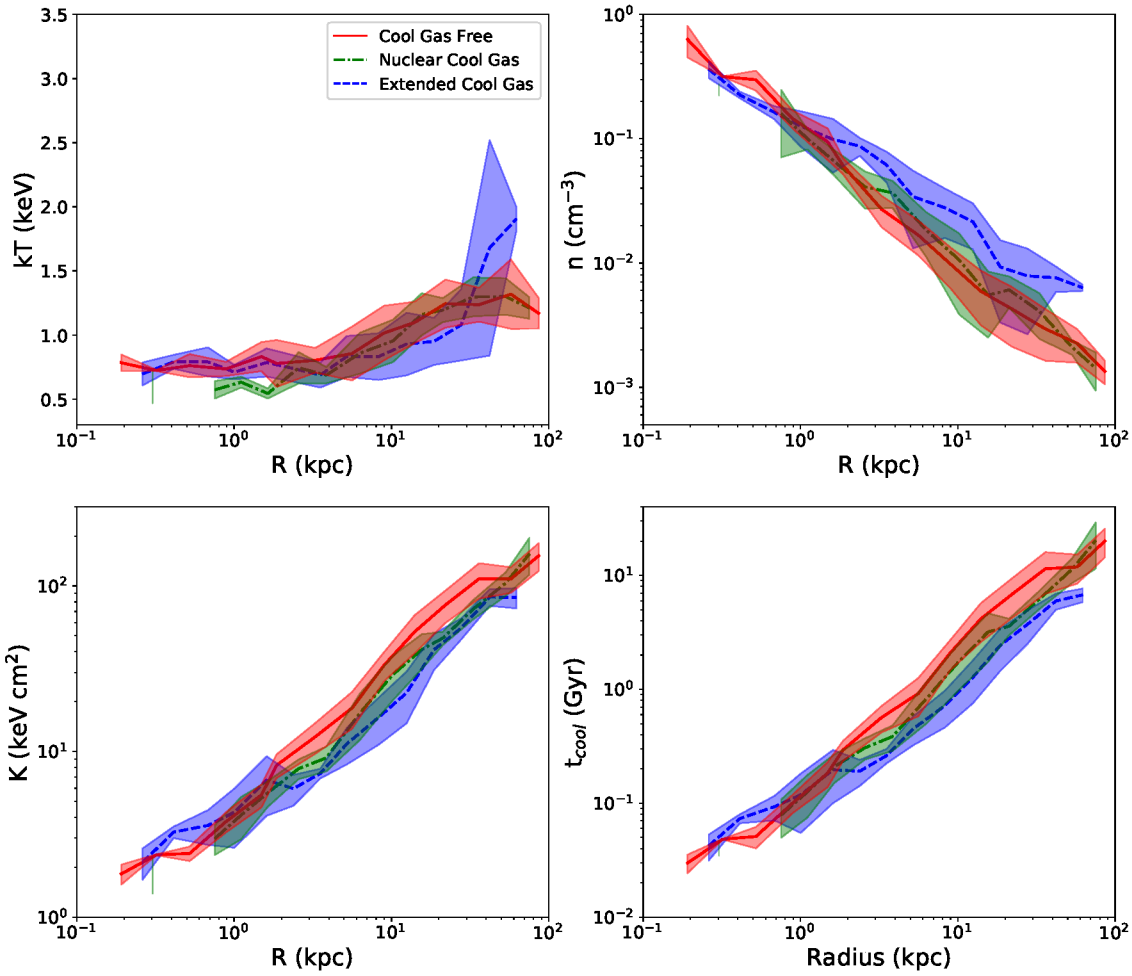

Figure 3. The combined radially binned profiles of temperature (top left), density (top right), entropy (bottom left) and cooling time (bottom right) for the full sample (see §3.2). The red (solid), green (dashed-dotted) and blue (dashed) lines show median profiles for the cool gas free, nuclear cool gas and extended cool gas systems, respectively and the shaded regions show the median absolute deviation (MAD) spreads about the medians. The figure shows higher densities and lower entropies and cooling times for the extended cool gas galaxies than the rest of the sample, outside the innermost regions (∼2 kpc).

Table 2. Results of the linear correlation analysis, discussed in §4.1, for the 0.5–7.0 keV X-ray luminosities (L_X; in erg s^{-1}), the total gas masses (M_{gas}; in $M_\odot$), the gas mass fractions (f_{gas}) and the Y_X (= $M_{gas}T_X$; in $M_\odot$ keV) values, estimated from within a radius of 10 kpc with the gas temperatures (T_X; in keV) determined from the same region (results also shown in Fig. 1).

Relation	Intercept	Slope	Corr. Coeff.
L_X-T_X	$(3.1\pm0.5)\times10^{41}$	3.1±0.5	0.67±0.09
M_{gas}-T_X	$(1.7\pm0.3)\times10^{9}$	2.6±0.5	0.63±0.10
f_{gas}-T_X	0.005±0.001	1.6±0.5	0.48±0.13
Y_X-T_X	$(1.7\pm0.3)\times10^{9}$	3.6±0.5	0.75±0.07

4 DISCUSSION

4.1 Cooling instabilities and the thermodynamic properties of galactic atmospheres

4.1.1 Correlation with average X-ray properties

The distributions of X-ray luminosities (L_X), gas masses (M_{gas}), gas mass fractions (f_{gas}) and the $Y_X = M_{gas}T_X$ values, within $r < 10$ kpc plotted vs. the average X-ray temperatures within the same region (obtained in §3.1), for the galaxies without and with different extents of cool gas are shown in Fig. 1. We obtained the gas mass estimates (M_{gas}) and the gas mass fractions (f_{gas}) for all the galaxies within the same 10 kpc radius circular regions. The gas masses were obtained by integrating the densities obtained in §3.2 ($M_{gas}(r) = \int 4\pi r^2 \mu m_H n\, dr$), and the gas mass fractions were obtained as $f_{gas}(r) = M_{gas}(r)/M_{tot}(r)$. The

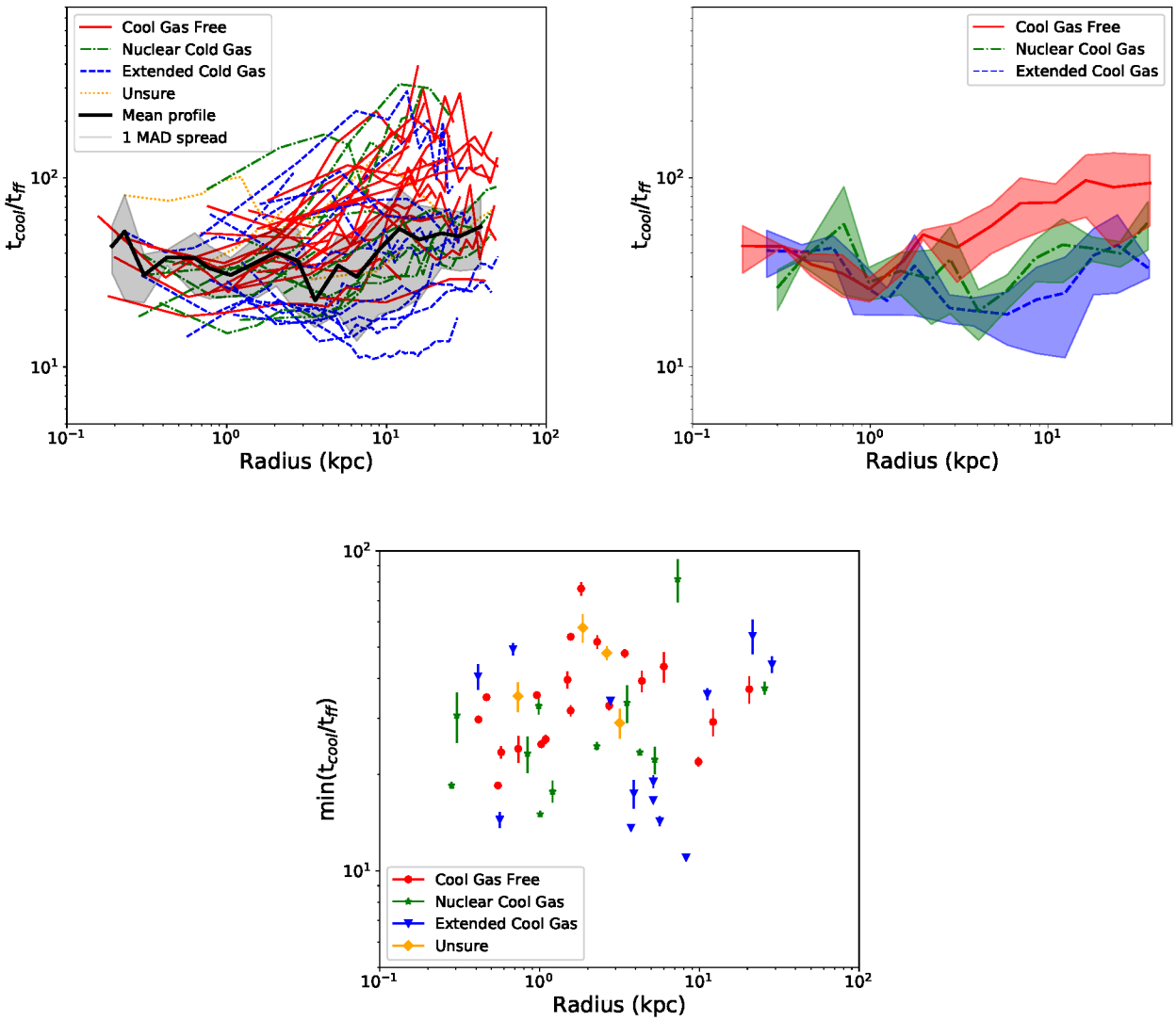

Figure 4. The $t_{\rm cool}/t_{\rm ff}$ profiles of the full sample (top left), the radially binned combined $t_{\rm cool}/t_{\rm ff}$ profiles of the different cold gas morphology groups (top right) and the min($t_{\rm cool}/t_{\rm ff}$) values of the full sample (bottom panel) (see §4.1). The red (solid lines/circles), green (dashed-dotted lines/stars), blue (dashed lines/triangles) and orange (dotted lines/diamonds) symbols denote the cool gas free, nuclear cool gas, extended cool gas and unsure systems, respectively. The black solid lines in the top left panel, and the red (solid), green (dashed-dotted) and blue (dashed) lines in the top right panel show the median profiles for the full sample, and the cool gas free, nuclear cool gas and extended cool gas galaxies, respectively. The shaded regions show the median absolute deviation (MAD) spreads about the medians. The presence of cool gas seems to be preferred in systems with lower values of min($t_{\rm cool}/t_{\rm ff}$).

total masses of the galaxies, $M_{\rm tot}(r)$ within a radius r, were obtained from the gas pressure gradients assuming hydrostatic equilibrium. The pressure gradients were determined using smooth empirical fits[3] to the pressure profiles obtained in §3.2. We do not see any trends in $L_{\rm X}$, $M_{\rm gas}$ and $f_{\rm gas}$ with the presence or morphology/extent of cool gas.

The linear correlation coefficients in log-space between $L_{\rm X}-T_{\rm X}$, $M_{\rm gas}-T_{\rm X}$, $f_{\rm gas}-T_{\rm X}$ and $Y_{\rm X}-T_{\rm X}$ were found to be 0.67±0.09, 0.63±0.10, 0.48±0.13 and 0.75±0.07 (obtained using the python *linmix* package), and the best-fit relations were found to be $L_{\rm X}\propto T_{\rm X}^{3.1\pm0.5}$, $M_{\rm gas}\propto T_{\rm X}^{2.6\pm0.5}$, $f_{\rm gas}\propto T_{\rm X}^{1.6\pm0.5}$, and $Y_{\rm X}\propto T_{\rm X}^{3.6\pm0.5}$, respectively. Our best-fit $L_{\rm X}-T_{\rm X}$ relation is shallower than that found in the group-cluster combined studies (e.g., see Kim & Fabbiano 2015; Goulding et al. 2016; Babyk et al. 2018b). However, the relation is fully consistent with the ones obtained using group only samples (Sun 2012; Bharadwaj et al. 2015). The results for all these linear correlations ($Y=AX^B$; in log space) viz., the intercepts (A), slopes (B) and correlation coefficients, are given in Table 2. The (weak) positive correlation between the gas mass fractions and the X-ray temperatures suggests that the cores of hotter, more massive systems are

[3] We tried three different models: a powerlaw, a beta model and a 4-parameter model, described in Lakhchaura et al. (2016).

able to hold on to a larger fraction of their X-ray emitting gas.

4.1.2 Correlation with thermodynamic profiles

The deprojected thermodynamic profiles shown in Figs. 2 and 3 show higher densities for the extended cool gas galaxies (blue) as compared to the cool gas free galaxies (red). The galaxies with extended cool gas are also found to have lower entropies and cooling times than their cool gas free counterparts, outside of their innermost regions (∼2 kpc). Using a subsample of 10 galaxies which are also included in this study, Werner et al. (2014) found a clear separation in the entropy profiles of galaxies with extended emission line filaments and cool gas free galaxies. In our study of a much larger sample, however, the separation is less clear and becomes more pronounced outside of the innermost regions at $r \gtrsim 2$ kpc.

The large scatter seen in the thermodynamic profiles is consistent with the short duty cycles (proportional to the cooling time at $r < 0.1\ R_{500}$; Gaspari & Sądowski 2017) predicted by the CCA-regulated feedback in early type galaxies. As suggested by NGC 6868, the few low-density (high-entropy) outliers with cool gas can be understood by the fact that they might possess significant rotation. This was also observed in the massive lenticular galaxy NGC 7049 which has a high central entropy, despite having a cool Hα+[NII] disk (see Juráňová et al. 2018). Rotation can strongly reduce the SMBH accretion rate (Gaspari et al. 2015), inducing a long-term accumulation of cold/warm gas in the central region or in an extended disc, thus making the multiphase state uncorrelated with the current hot halo properties. The presence of rotational support can decrease the gravitational potential depth and hence, the X-ray surface-brightness. This has also been observed in simulations. Based on 2D high-resolution hydrodynamic simulations of early type galaxies, Negri et al. (2014) found that the hot X-ray emitting gas in fast-rotating galaxies has a systemically lower surface brightness than the hot gas in the non-rotating systems of similar masses. The effect has also been found in some other studies (Brighenti & Mathews 1996; Gaspari et al. 2015; Gaspari & Sądowski 2017).

Using numerical simulations it has been found that thermal instability is only significant when the cooling time of the gas is less than ∼ 10 free-fall times (see Sharma et al. 2012; McCourt et al. 2012; Gaspari et al. 2012b, 2013; Meece et al. 2015). We calculated the profiles of free fall time for all our galaxies as $t_{\rm ff} = \sqrt{2r/g}$; where the acceleration due to gravity $g = d\phi/dr = 2\sigma_{\rm c}^2/r$ (assuming an isothermal sphere potential $\phi = 2\sigma_{\rm c}^2\ log(r) + const.$), leading to $t_{\rm ff} = r/\sigma_{\rm c}$; where $\sigma_{\rm c}$ is the mean central velocity dispersion obtained from the Hyperleda database (Makarov et al. 2014).[4].

The $t_{\rm cool}/t_{\rm ff}$ profiles of the individual galaxies are shown in Fig. A.6. The $t_{\rm cool}/t_{\rm ff}$ profiles and the minimum values of $t_{\rm cool}/t_{\rm ff}$, for the full sample are shown in the top left and bottom panels of Fig. 4, respectively. In the top right panel we also show the median $t_{\rm cool}/t_{\rm ff}$ profiles of the cool gas free (red solid lines), nuclear cool gas (green dashed-dotted lines) and extended cool gas (blue dashed lines) groups with the shaded regions showing the median absolute deviation about the median profiles. The figure shows that galaxies with cool gas emission (extended+nuclear) have in general, lower values of $t_{\rm cool}/t_{\rm ff}$ than the cool gas free galaxies (red), especially outside the innermost regions (∼3 kpc). There seems to be a separation in the $t_{\rm cool}/t_{\rm ff}$ values of the cool gas rich (nuclear and extended) galaxies and the cool gas free galaxies outside ∼3 kpc. Also, the $t_{\rm cool}/t_{\rm ff}$ profiles of the extended cool gas galaxies seem to be flatter in the 3-10 kpc range as compared to the nuclear cool gas and cool gas free galaxies for which the values seem to be increasing with radius.

4.1.3 Distributions of cooling instability criteria

We fitted powerlaw models to the entropy profiles ($K = K_{10}\,(r/10)^{\alpha_{\rm K}}$) of all the galaxies in the radial range of 1–30 kpc. A histogram of the entropies of the individual galaxies at 10 kpc (K_{10}) obtained from the fits, is shown in the top left panel of Fig. 5. The histogram shows that the galaxies with extended emission line nebulae have lower K_{10} values than the cool gas free galaxies. However, there are outliers and we do not see a clear demarcation in the entropy between the galaxies with and without ongoing cooling, which is also expected because of the short duty cycles of these galaxies. The mean±sigma K_{10} values obtained from a Gaussian fitting of the K_{10} histograms obtained for the cool gas free and the extended cool gas groups were 34±10 keV cm^2 and 24±7 keV cm^2, respectively. The top right panel of Fig. 5 shows histograms of the minimum values of $t_{\rm cool}/t_{\rm ff}$ obtained for the cool gas free and cool gas rich (extended+nuclear cool gas) groups, which show a similar trend as the entropy. The mean±sigma min($t_{\rm cool}/t_{\rm ff}$) values obtained from Gaussian fitting of the histograms obtained for the cool gas free and cool gas rich (extended+nuclear) groups were 36±13 and 29±16, respectively.

According to Voit et al. (2017), the formation of cooling instabilities also depends on the slopes of entropy profiles. The histograms of the slopes $\alpha_{\rm K}$, of the best power-law fits to the entropy distributions of the cool gas free and extended cool gas groups are shown in the bottom left panel of Fig. 5. The separation of the two groups appears much weaker here than for the other parameters. The mean±sigma $\alpha_{\rm K}$ values obtained from Gaussian fitting of the histograms for the cool gas free and extended cool gas groups were 0.86±0.20 and 0.75±0.20, respectively.

McNamara et al. (2016), Gaspari & Sądowski (2017) and Gaspari et al. (2018) argue that uplift and turbulent

[4] We also tried calculating g assuming hydrostatic equilibrium, $g = -\rho^{-1}dP/dr$ (ρ = gas mass density = $\mu n m_p$; μ =0.62; m_p=proton mass), obtained using smooth empirical fits to the pressure profiles. The contribution of non-thermal pressure in a small sub-sample of galaxies was checked by implementing the approach used in Churazov et al. (2010). We found a maximum non-thermal pressure support of ∼ 30%. Therefore, for the small radial distances concerned in this paper where the non-thermal pressure can be really significant, we decided to use g obtained using the isothermal sphere potential. We found that using the latter method the $t_{\rm cool}/t_{\rm ff}$ values decrease in the outer regions and increase in the inner regions, although the min($t_{\rm cool}/t_{\rm ff}$) values are only slightly affected

motions promote nonlinear condensation[5]. To estimate the disturbedness in our systems, which might be an indication of the level of gas motions, we did the following. We first produced 0.5–7.0 keV exposure-corrected images for all the galaxies. Point sources were detected, removed and the empty regions were filled with the average counts from the neighboring pixels. The images were then smoothed with Gaussians of 3 pixel (∼1.5") width and were fitted with 2D double β-models in the *CIAO Sherpa* package. As a proxy for the gas motions (e.g., Hofmann et al. 2016; Gaspari & Churazov 2013; Zhuravleva et al. 2014), we use the root-mean-square (RMS) fluctuations of the residual images within the central 5 kpc regions.

The histograms of the RMS fluctuations obtained for the cool gas rich (extended+nuclear) and cool gas free galaxies, are shown in the right bottom panel of Fig. 5. Although the plot does not show a clear demarcation value of RMS fluctuations between the cool gas rich and free galaxies, it can be seen that in general, the formation of cooling instabilities is preferred in galaxies with higher RMS fluctuations. We also tried the scales at 2.5 kpc and 10 kpc. The distinction between cool gas free and cool gas rich galaxies seems to get better at smaller scales (2.5 kpc) and almost disappears at larger scales (10 kpc). The mean±sigma 5 kpc RMS fluctuations obtained from the Gaussian fitting to the histograms for the cool gas free and cool gas rich (extended+nuclear) groups was found to be 0.02±0.01 and 0.03±0.02, respectively. Note that the value of the RMS fluctuation has some dependence also on the depth of the data and the pixel scale, and the line of sight projection effects also complicate these measurements.

We also checked if the K_{10}, $\min(t_{\rm cool}/t_{\rm ff})$, $\alpha_{\rm K}$ and RMS fluctuations obtained for the cool gas rich and cool gas poor galaxies statistically belong to two different populations. For this we used Welch's t-test where t is defined as

$$t = (\overline{X_1} - \overline{X_2})/\sqrt{\frac{S_1^2}{n_1} + \frac{S_2^2}{n_2}} \qquad (2)$$

; where $\overline{X_1}$ and $\overline{X_2}$ are the means, S_1^2 and S_2^2 are the variances and n_1 and n_2 are the sizes of the two samples X_1 and X_2. The test is based on the null-hypothesis that the samples have been taken from the same parent distribution. The t values so obtained and the corresponding null hypothesis probabilities (p for $n_1 + n_2 - 2$ degrees of freedom), for the K_{10}, $\min(t_{\rm cool}/t_{\rm ff})$, $\alpha_{\rm K}$ and RMS fluctuations obtained for the extended cool gas (ECG), Nuclear cool gas (NCG) and Cool gas free (CGF) groups, using different combinations (viz., ECG vs. CGF, ECG+NCG vs. CGF and ECG vs. NCG+CGF) of the three groups, are given in Table 3. The histograms of K_{10}, $\min(t_{\rm cool}/t_{\rm ff})$, $\alpha_{\rm K}$ and RMS fluctuations corresponding to only the best combination (highest t, lowest p) are shown in Fig. 5. We find that the distributions of K_{10}, $\min(t_{\rm cool}/t_{\rm ff})$, $\alpha_{\rm K}$ and the RMS fluctuations of the cool gas-rich and cool gas-free galaxies are different at >99%, 91%, 87% and 98% confidence levels, respectively.

[5] Note that this is a more direct and efficient way to produce multiphase gas, since linear thermal instability models (linked to $t_{\rm cool}/t_{\rm ff}$) require tiny perturbations to grow nonlinear against the restoring buoyancy force. Furthermore, we note that, in a tightly self-regulated loop, the cool gas is also agent of higher SMBH accretion rates, which will later produce jets and maintain a significant level of turbulent/RMS fluctuations (cf., Gaspari et al. 2012a,b).

Table 3. The results of the Welch's t-test for the K_{10}, $\min(t_{\rm cool}/t_{\rm ff})$, $\alpha_{\rm K}$ and RMS fluctuation values obtained for the extended cool gas (ECG), Nuclear cool gas (NCG) and Cool gas free (CGF) groups. We used different combinations (viz., ECG vs. CGF, ECG+NCG vs. CGF and ECG vs. NCG+CGF) for the samples X_1 and X_2 with means $\overline{X_1}$ and $\overline{X_2}$ and variances S_1^2 and S_2^2, respectively. The t-values and null hypothesis (viz. both samples were taken from the same parent distribution) probabilities (p), and the degrees of freedom (DOF) are calculated as defined in §4.1.3.

K_{10}						
X_1	X_2	$\overline{X_1} \pm S_1$ (keV cm^2)	$\overline{X_2} \pm S_2$ (keV cm^2)	t	DOF	p
ECG	CGF	24±7	34±10	3.20	31	0.003
ECG+NCG	CGF	27±12	34±10	2.01	43	0.05
ECG	CGF+NCG	24±7	33±12	2.78	43	0.008
$\min(t_{\rm cool}/t_{\rm ff})$						
X_1	X_2	$\overline{X_1} \pm S_1$	$\overline{X_2} \pm S_2$	t	DOF	p
ECG	CGF	28±15	36±13	1.53	31	0.14
ECG+NCG	CGF	29±16	36±13	1.75	43	0.09
ECG	CGF+NCG	28±15	34±15	1.14	43	0.26
$\alpha_{\rm K}$						
X_1	X_2	$\overline{X_1} \pm S_1$	$\overline{X_2} \pm S_2$	t	DOF	p
ECG	CGF	0.75±0.20	0.86±0.20	1.56	31	0.13
ECG+NCG	CGF	0.78±0.23	0.86±0.20	1.23	43	0.20
ECG	CGF+NCG	0.75±0.20	0.85±0.22	1.38	43	0.17
RMS fluctuation						
X_1	X_2	$\overline{X_1} \pm S_1$	$\overline{X_2} \pm S_2$	t	DOF	p
ECG	CGF	0.03±0.01	0.02±0.01	2.26	31	0.03
ECG+NCG	CGF	0.03±0.02	0.02±0.01	2.45	43	0.02
ECG	CGF+NCG	0.03±0.01	0.02±0.22	1.22	43	0.23

4.2 Feedback cycles

To investigate the connection between the cool gas and AGN activity, we search for a correlation between the AGN jet power and the Hα+[NII] luminosities of the galaxies. The jet powers ($P_{\rm jet}$) are calculated as the work required to inflate a cavity with a volume V divided by the age of the cavity, $P_{\rm jet} = 4PV/t_{\rm age}$. P is the pressure of the hot gas determined from the X-ray observations. Cavities are usually approximated as ellipsoids and their sizes are estimated either from the X-ray images (Cavagnolo et al. 2010; Russell et al. 2013) or from the radio lobes (Allen et al. 2006). The ages of cavities are either assumed to be their buoyancy rise times or sound crossing times $r/c_{\rm s}$ (where r is the distance of the cavity from the centre and $c_{\rm s}$ is the sound speed).

Due to the inconsistencies in the $P_{\rm jet}$ estimates available in the literature, we recalculated these values for 15 of the 21 galaxies in our sample that host clear cavities. The sizes for all these cavities (except for NGC 4649) were taken from a single source, Shin et al. (2016). For NGC 4649, we used the X-ray cavity size given in Paggi et al. (2014). The cavity volumes and the associated uncertainties were calculated

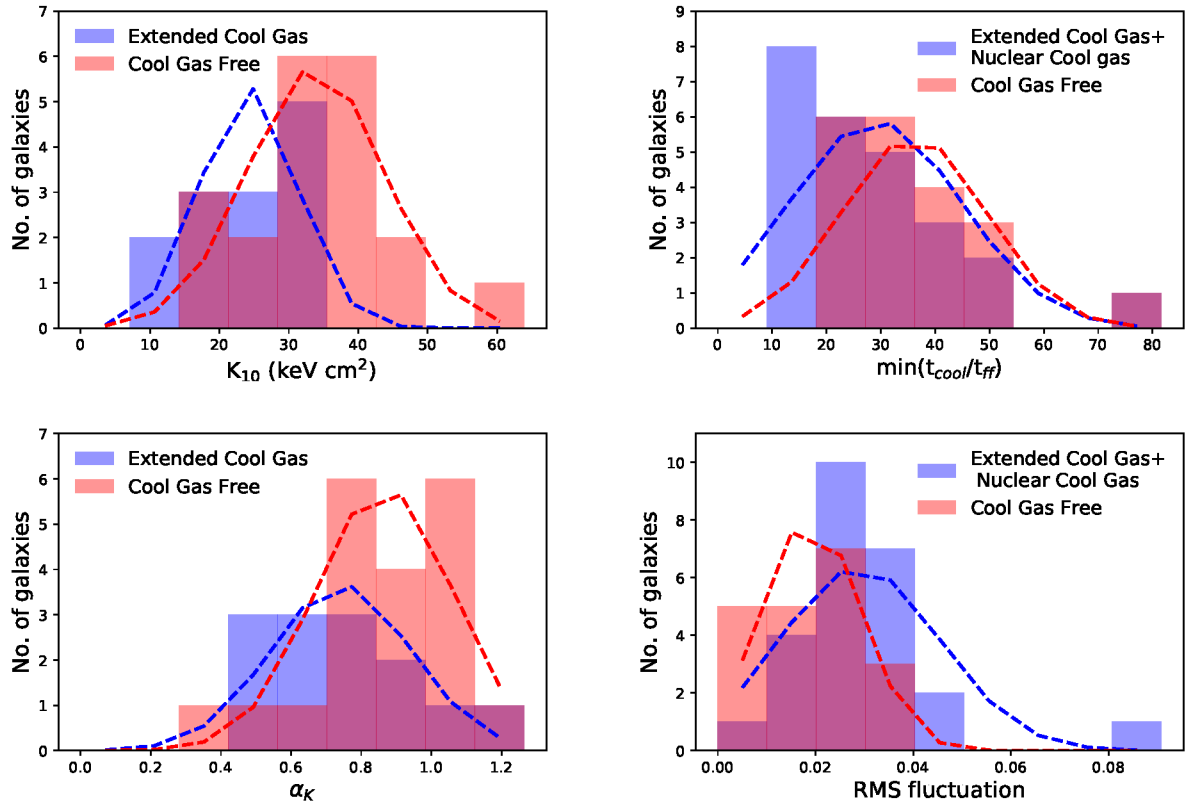

Figure 5. The histograms of K_{10}, $\min(t_{\rm cool}/t_{\rm ff})$, $\alpha_{\rm K}$ and RMS fluctuation, described in §4.1. The blue and red colors denote the cool gas rich and cool gas poor systems, respectively, and the dotted line shows the best-fitting Gaussians for the two groups. The presence of cool gas seems to be preferred in systems with lower values of K_{10}, $\min(t_{\rm cool}/t_{\rm ff})$, $\alpha_{\rm K}$ and high RMS fluctuations.

as described in Bîrzan et al. (2004). The ages of the cavities were estimated as their buoyancy rise times. For the remaining 6 galaxies with cavities, we used the estimates given in Cavagnolo et al. (2010), as their method of calculating jet powers is similar to ours. The jet powers for the 21 galaxies are given in Table 4.

Fig. 6 shows the jet powers for the 21 galaxies as a function of their Hα+[NII] luminosities. For six of the 21 galaxies, the Hα+[NII] luminosities were obtained from Macchetto et al. (1996); five of these were detected as small disk emission. Also, there were three more galaxies for which Hα+[NII] flux estimates were available in the literature but no Hα+[NII] emission was detected in the SOAR/APO observations. As discussed in §2.1, the Hα+[NII] luminosities for these eight sources should be interpreted as upper-limits. We find a weak positive correlation (Pearson's coefficient $\sim$0.38) between the two quantities, which reduces to $\sim$0.24, if the eight galaxies with upper limits are excluded. From Fig. 6, in general, the jet power seems to be increasing with the increase in the cool gas extent and is the strongest for the galaxies with the most extended Hα+[NII] filaments, such as NGC 5044, NGC 4696 and NGC 533.

Of the 15 galaxies, for which we recalculated the jet powers, the estimate for NGC 4261 was found to be too low. The galaxy, however, hosts very powerful jets (see O'Sullivan et al. 2011). Therefore, we also recalculated the correlation coefficient using the lower limit for the jet power in this system from O'Sullivan et al. (2011) (cavity sizes estimated using radio lobes). With this, we find a weak positive correlation (Pearson's coefficient $\sim$0.19) between the two quantities which reduces to $\sim$-0.04, if the eight galaxies with upper limits are excluded.

The large scatter in the jet powers and the Hα+[NII] luminosities, the positive correlation between the two, and the increase of jet power with the cool gas extent, hint toward the scenario of hysteresis cycles driven by CCA, which has been shown via high-resolution 3D hydrodynamic simulations to be the most consistent mechanism for self-regulating AGN feedback in ETGs (cf., Gaspari et al. 2013, 2015, 2018) and brightest cluster galaxies (cf., Gaspari et al. 2012a,b; Prasad et al. 2015; Voit et al. 2017). Simply put, during CCA, the higher the condensed gas mass (thus higher $L_{\rm H\alpha+[NII]}$), the stronger the SMBH accretion rate, and thus feedback power ($P_{\rm feed} \propto \dot{M}_{\rm cool}\, c^2$; more below). On top of this trend, the intrinsically chaotic evolution of the colliding clouds/filaments in CCA drives a substantial ($\sim$ 1 dex) variability which can hinder a strong linear correlation (yet preserving a positive Pearson coefficient). Furthermore, the correlation between $P_{\rm jet}$ and cool gas luminosity (thus condensation) is consistent with the turbulent eddy criterion (§1), as larger jet powers imply larger turbulent velocity dispersions (from the turbulent energy flux rate, $\sigma_v \propto P_{\rm jet}^{1/3}$) and hence larger RMS surface brightness fluctuations (as found in §4.1.3). We note that alternative models as hot/Bondi accretion would instead have negligible variability and show

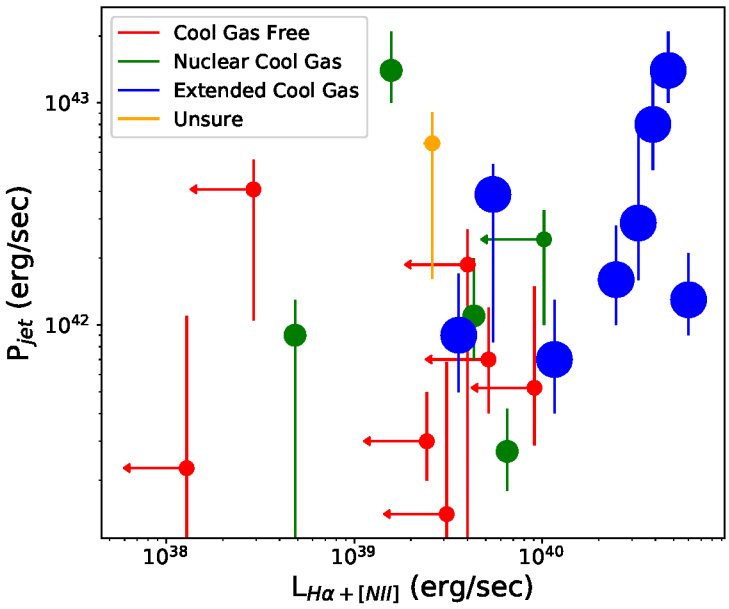

Figure 6. Jet powers of the 21 galaxies with X-ray cavities vs. their Hα+[NII] luminosities (bigger circles represent more extended Hα+[NII] emission). The red, green, blue and orange colors denote the cool gas free, nuclear cool gas, extended cool gas and unsure systems, respectively. There seems to be a weak positive correlation between the AGN jet powers of the galaxies and their Hα+[NII] luminosities.

no correlations with the cool phase (nor turbulence). Needless to say, forthcoming investigations should significantly expand the ETG sample and achieve more accurate detections in warm gas, which remains one of our main thrusts for our ongoing campaigns.

In more detail, the AGN self-regulation cycle works as follows. In the beginning of the proposed AGN feedback cycle, the galaxies have, in general, weak gas motions and smooth and symmetric X-ray morphologies. Galaxies in this phase have neither cold gas nor central AGN jets but may have high central entropies as a result of past AGN activity. As the gas in the central regions of the galaxies cools, the entropy decreases and the cooling instabilities start forming, giving rise to the cold gas filaments. As the cold gas accretion increases, the AGN jet power also increases and the powerful jets start interacting with the surrounding medium, driving large scale gas motions and inflating X-ray cavities. The gas motions further increase the formation of cooling instabilities. Eventually, the jets start heating the surrounding medium[6], preventing further formation of cold gas and might also destroy the existing cold gas filaments. The cold gas fuel further reduces due to the AGN jet interaction and the galaxies might then be left with just nuclear cold gas with some AGN activity. Finally due to the lack/absence of cold gas fuel, the AGN starves, the jet activity stops and the galaxy returns to its initial phase.

[6] We note that the hysteresis cycling mainly occurs within the core region ($<$ 10 kpc, for both initially low or high K_{100} systems), while AGN jet feedback rarely affects the large-scale 100 kpc profiles over the Gyr evolution (e.g., Wang et al. 2018).

As also discussed in §4.1, it is important to note that the feedback cycles in early type galaxies are much faster (a few 10s Myr) compared to massive clusters (several 100s Myr). Note also how the cooling rate $\dot{M}_{\rm cool} \propto L_{\rm X}/T_{\rm X}$ is *relatively* larger in massive ETGs because of line cooling (<1 keV) and the $T_{\rm x}^{-1}$ dependence. This implies a much more pronounced hysteresis in the early type galaxies, with high/low feeding and feedback states less separated and more intertwined, as found in the current observational study.

Based on an analysis of 107 galaxies, groups and clusters, McDonald et al. (2018) found that the correlation between the mass cooling rate of the ICM and the star formation rate breaks down at the low mass end, suggesting that the cold gas and star formation are mainly being driven by stellar mass loss for the low mass systems. However, in our sample, majority of which includes massive ETGs with extended halos, we see clear separations in the density, entropy, and cooling time profiles in the 2-35 kpc radial range, based on the multiphase gas presence. These are clear signs of large-scale condensation.

Elliptical galaxies, groups and poor clusters of galaxies are the building blocks of massive clusters and are, therefore, crucial for understanding the cosmic structure formation in the Universe. Moreover, X-ray halos are of key importance and appear to be ubiquitous, not only for massive ETGs but even for compact or fossil ETGs (e.g., Werner et al. 2018). As of now, most of the studies centred on the non-gravitational processes (cooling, AGN feedback etc.) focus only on the bright massive clusters since the current X-ray missions are limited in their capability to study the X-ray emission in the fainter low mass systems out to R_{500}. The future *Athena* X-ray observatory will allow us to extend the

Table 4. AGN jet power ($P_{\rm jet}$) estimates for 21 galaxies of the sample.

Target Name	$P_{\rm jet}$ (10^{43} erg/sec)	Ref.*
IC 4296	$0.39^{+0.14}_{-0.30}$	C
NGC 315	$0.66^{+0.25}_{-0.50}$	C
NGC 533	$0.29^{+0.55}_{-0.13}$	P
NGC 777	$0.41^{+0.15}_{-0.30}$	C
NGC 1316	$0.05^{+0.14}_{-0.03}$	P
NGC 1399	$0.02^{+0.09}_{-0.02}$	P
NGC 1407	$0.01^{+0.05}_{-0.01}$	P
NGC 1600	$0.19^{+0.08}_{-0.20}$	C
NGC 4261	$0.09^{+0.04}_{-0.08}$	P
	>1.0	O
NGC 4374	$0.20^{+0.48}_{-0.11}$	P
NGC 4472	$0.02^{+0.03}_{-0.01}$	P
NGC 4486	$0.44^{+0.31}_{-0.06}$	P
NGC 4552	$0.01^{+0.01}_{-0.001}$	P
NGC 4636	$0.11^{+0.11}_{-0.03}$	P
NGC 4649	$0.05^{+0.10}_{-0.02}$	P
NGC 4696	$0.57^{+0.55}_{-0.08}$	P
NGC 4782	$0.24^{+0.09}_{-0.14}$	C
NGC 5044	$0.51^{+1.25}_{-0.29}$	P
NGC 5813	$0.58^{+1.25}_{-0.27}$	P
NGC 5846	$0.11^{+0.13}_{-0.02}$	P
NGC 4778	$0.70^{+1.68}_{-0.37}$	P

* C: Cavagnolo et al. (2010), O: O'Sullivan et al. (2011), P: Present Work.

studies of hot halos in giant elliptical galaxies out to redshift $z \sim 1$, allowing us to investigate the various details (source, effect mass dependence, timescales etc.) of the non-gravitational processes (Ettori et al. 2013; Roncarelli et al. 2018).

5 CONCLUSIONS

We have analysed *Chandra* X-ray observations of a sample of 49 nearby X-ray and optically bright giant elliptical galaxies. In particular, we focus on the connection between the properties of the hot X-ray emitting gas and the cooler Hα+[NII] emitting phase, and the possible role of the cool phase in the AGN feedback cycle. Our main findings are summarised as follows:

- We do not find a correlation between the presence of Hα+[NII] emission and the X-ray luminosity, mass of hot gas, and gas mass fraction.
- The observed correlation between the gas mass fractions and the X-ray temperatures suggests that the cores of hotter, more massive systems are able to hold on to a larger fraction of their X-ray emitting gas.
- We find that the presence of Hα+[NII] emission is more likely in systems with higher densities, lower entropies and cooling times (outside the innermost regions) shallower entropy profiles, lower values of $\min(t_{\rm cool}/t_{\rm ff})$, and more disturbed X-ray morphologies.
- The distributions of the thermodynamic properties of the nuclear cool gas galaxies are found to be in between the extended cool gas and cool gas free galaxies.
- We find that the distributions of entropies at 10 kpc, the $\min(t_{\rm cool}/t_{\rm ff})$ values, the slope of the entropy profiles ($\alpha_{\rm K}$) and the RMS surface-brightness fluctuations within a radius of 5 kpc are statistically different between cool gas-rich and cool gas-free galaxies at >99%, 91%, 87% and 98% confidence levels, respectively.
- The large scatter and the significant overlap between the properties of systems with and without optical emission line nebulae, indicate rapid transitions from one group to the other. The continuous distribution might also be a result of the chaotic nature and rapid variability of the feeding and feedback cycle in these systems.
- The AGN jet power of the galaxies with X-ray cavities hint toward a positive correlation with their Hα+[NII] luminosity. This feature, the presence of cool gas in more disturbed/turbulent halos, and frequent hysteresis cycles in ETGs are consistent with a cold gas nature of AGN feeding and related CCA scenario.

ACKNOWLEDGEMENTS

This work was supported by the Lendulet LP2016-11 grant awarded by the Hungarian Academy of Sciences. M.S. is supported by NSF grant 1714764, Chandra grant AR7-18016X and NASA grant NNX15AK29A. M.G. is supported by NASA through Einstein Postdoctoral Fellowship Award Number PF5-160137 issued by the Chandra X-ray Observatory Center, which is operated by the SAO for and on behalf of NASA under contract NAS8-03060. Support for this work was also provided by Chandra grant GO7-18121X. C.S. is supported in part by Chandra grants GO5-16146X, GO7-18122X, and GO8-19106X. R.E.A.C. is supported by NASA through Einstein Postdoctoral Fellowship Award Number PF5-160134 issued by the Chandra X-ray Observatory Center, which is operated by the SAO for and on behalf of NASA under contract NAS8-03060. The scientific results reported in this article are based to a significant degree on data obtained from the *Chandra Data Archive*. This research has made use of software provided by the *Chandra X-ray Centre* (CXC) in the application packages CIAO, CHIPS and Sherpa. This research has made use of data, software and web tools obtained from the High Energy Astrophysics Science Archive Research Center (HEASARC), a service of the Astrophysics Science Division at NASA/GSFC and of the Smithsonian Astrophysical Observatory's High Energy Astrophysics Division. Based on observations obtained at the Southern Astrophysical Research (SOAR) telescope, which is a joint project of the Ministério da Ciência, Tecnologia, Inovações e Comunicações (MCTIC) do Brasil, the U.S. National Optical Astronomy Observatory (NOAO), the University of North Carolina at Chapel Hill (UNC), and Michigan State University (MSU). Based on observations obtained with the Apache Point Observatory 3.5-meter telescope, which is owned and operated by the Astrophysical Research Consortium.

REFERENCES

Allen S. W., Dunn R. J. H., Fabian A. C., Taylor G. B., Reynolds C. S., 2006, MNRAS, 372, 21

Annibali F., Bressan A., Rampazzo R., Zeilinger W. W., Vega O., Panuzzo P., 2010, A&A, 519, A40

Arnaud K. A., 1996, in Jacoby G. H., Barnes J., eds, Astronomical Society of the Pacific Conference Series Vol. 101, Astronomical Data Analysis Software and Systems V. p. 17

Babyk I. V., McNamara B. R., Nulsen P. E. J., Russell H. R., Vantyghem A. N., Hogan M. T., Pulido F. A., 2018a, preprint, (arXiv:1802.02589)

Babyk I. V., McNamara B. R., Nulsen P. E. J., Hogan M. T., Vantyghem A. N., Russell H. R., Pulido F. A., Edge A. C., 2018b, ApJ, 857, 32

Bharadwaj V., Reiprich T. H., Lovisari L., Eckmiller H. J., 2015, A&A, 573, A75

Bîrzan L., Rafferty D. A., McNamara B. R., Wise M. W., Nulsen P. E. J., 2004, ApJ, 607, 800

Blanton E. L., Sarazin C. L., McNamara B. R., Clarke T. E., 2004, ApJ, 612, 817

Bower G. A., Heckman T. M., Wilson A. S., Richstone D. O., 1997, ApJ, 483, L33

Brighenti F., Mathews W. G., 1996, ApJ, 470, 747

Brown M. J. I., Jannuzi B. T., Floyd D. J. E., Mould J. R., 2011, ApJ, 731, L41

Buote D. A., 2000, MNRAS, 311, 176

Caon N., Macchetto D., Pastoriza M., 2000, ApJS, 127, 39

Cavagnolo K. W., Donahue M., Voit G. M., Sun M., 2009, ApJS, 182, 12

Cavagnolo K. W., McNamara B. R., Nulsen P. E. J., Carilli C. L., Jones C., Bîrzan L., 2010, ApJ, 720, 1066

Churazov E., et al., 2010, MNRAS, 404, 1165

Condon J. J., Cotton W. D., Greisen E. W., Yin Q. F., Perley R. A., Taylor G. B., Broderick J. J., 1998, AJ, 115, 1693

Condon J. J., Cotton W. D., Broderick J. J., 2002, AJ, 124, 675

Connor et al. 2018, in prep.

Cowie L. L., Hu E. M., Jenkins E. B., York D. G., 1983, ApJ, 272, 29

Crawford C. S., Allen S. W., Ebeling H., Edge A. C., Fabian A. C., 1999, MNRAS, 306, 857

David L. P., Jones C., Forman W., Nulsen P., Vrtilek J., O'Sullivan E., Giacintucci S., Raychaudhury S., 2009, ApJ, 705, 624

Donahue M., Stocke J. T., Gioia I. M., 1992, ApJ, 385, 49

Donahue M., Mack J., Voit G. M., Sparks W., Elston R., Maloney P. R., 2000, ApJ, 545, 670

Dunn R. J. H., Allen S. W., Taylor G. B., Shurkin K. F., Gentile G., Fabian A. C., Reynolds C. S., 2010, MNRAS, 404, 180

Edge A. C., 2001, MNRAS, 328, 762

Edge A. C., Frayer D. T., 2003, ApJ, 594, L13

Edge A. C., Wilman R. J., Johnstone R. M., Crawford C. S., Fabian A. C., Allen S. W., 2002, MNRAS, 337, 49

Edge A. C., et al., 2010, A&A, 518, L46

Ettori S., et al., 2013, preprint, (arXiv:1306.2322)

Fabian A. C., 2012, ARA&A, 50, 455

Fabian A. C., et al., 2016, MNRAS, 461, 922

Falcke H., Rieke M. J., Rieke G. H., Simpson C., Wilson A. S., 1998, ApJ, 494, L155

Ferrarese L., Ford H. C., Jaffe W., 1996, ApJ, 470, 444

Fruscione A., et al., 2006, in Society of Photo-Optical Instrumentation Engineers (SPIE) Conference Series. p. 62701V, doi:10.1117/12.671760

Gaspari M., Churazov E., 2013, A&A, 559, A78

Gaspari M., Sądowski A., 2017, ApJ, 837, 149

Gaspari M., Brighenti F., Temi P., 2012a, MNRAS, 424, 190

Gaspari M., Ruszkowski M., Sharma P., 2012b, ApJ, 746, 94

Gaspari M., Ruszkowski M., Oh S. P., 2013, MNRAS, 432, 3401

Gaspari M., Brighenti F., Temi P., 2015, A&A, 579, A62

Gaspari M., et al., 2018, ApJ, 854, 167

Gavazzi G., Boselli A., 1996, Astrophysical Letters and Communications, 35, 1

Gavazzi G., Boselli A., Vílchez J. M., Iglesias-Paramo J., Bonfanti C., 2000, A&A, 361, 1

Gebhardt K., et al., 2000, ApJ, 543, L5

González-Martín O., Masegosa J., Márquez I., Guainazzi M., Jiménez-Bailón E., 2009, A&A, 506, 1107

Goulding A. D., et al., 2016, ApJ, 826, 167

Grevesse N., Sauval A. J., 1998, Space Sci. Rev., 85, 161

Grossovà et al. 2018, in prep.

Hatch N. A., Crawford C. S., Fabian A. C., Johnstone R. M., 2005, MNRAS, 358, 765

Heckman T. M., Baum S. A., van Breugel W. J. M., McCarthy P., 1989, ApJ, 338, 48

Ho L. C., Filippenko A. V., Sargent W. L. W., 1997, ApJ, 487, 579

Hofmann F., Sanders J. S., Nandra K., Clerc N., Gaspari M., 2016, A&A, 585, A130

Hogan M. T., et al., 2017, ApJ, 851, 66

Irwin J. A., Athey A. E., Bregman J. N., 2003, ApJ, 587, 356

Jaffe W., Bremer M. N., 1997, MNRAS, 284, L1

Jaffe W., Bremer M. N., Baker K., 2005, MNRAS, 360, 748

Johnstone R. M., Fabian A. C., Nulsen P. E. J., 1987, MNRAS, 224, 75

Johnstone R. M., Hatch N. A., Ferland G. J., Fabian A. C., Crawford C. S., Wilman R. J., 2007, MNRAS, 382, 1246

Juráňová A., et al., 2018, preprint, (arXiv:1808.05761)

Kim D.-W., Fabbiano G., 2015, ApJ, 812, 127

Kuehr H., Witzel A., Pauliny-Toth I. I. K., Nauber U., 1981, A&AS, 45, 367

Kulkarni S., Sahu D. K., Chaware L., Chakradhari N. K., Pandey S. K., 2014, New Astron., 30, 51

Laing R. A., Peacock J. A., 1980, MNRAS, 190, 903

Lakhchaura K., Saini T. D., Sharma P., 2016, MNRAS, 460, 2625

Lauberts A., Valentijn E. A., 1989, The surface photometry catalogue of the ESO-Uppsala galaxies

Lim J., Ohyama Y., Chi-Hung Y., Dinh-V-Trung Shiang-Yu W., 2012, ApJ, 744, 112

Macchetto F., Pastoriza M., Caon N., Sparks W. B., Giavalisco M., Bender R., Capaccioli M., 1996, A&AS, 120, 463

Mackie G., Fabbiano G., 1998, AJ, 115, 514

Makarov D., Prugniel P., Terekhova N., Courtois H., Vauglin I., 2014, A&A, 570, A13

Mazzarella J. M., Madore B. F., Helou G., 2001, in Starck J.-L., Murtagh F. D., eds, Proc. SPIEVol. 4477, Astronomical Data Analysis. pp 20–34 (arXiv:astro-ph/0111200), doi:10.1117/12.447177

McCourt M., Sharma P., Quataert E., Parrish I. J., 2012, MNRAS, 419, 3319

McDonald M., Veilleux S., Rupke D. S. N., Mushotzky R., 2010, ApJ, 721, 1262

McDonald M., Wei L. H., Veilleux S., 2012, ApJ, 755, L24

McDonald M., Gaspari M., McNamara B. R., Tremblay G. R., 2018, ApJ, 858, 45

McNamara B. R., Nulsen P. E. J., 2012, New Journal of Physics, 14, 055023

McNamara B. R., Russell H. R., Nulsen P. E. J., Hogan M. T., Fabian A. C., Pulido F., Edge A. C., 2016, ApJ, 830, 79

Meece G. R., O'Shea B. W., Voit G. M., 2015, ApJ, 808, 43

Mittal R., et al., 2011, MNRAS, 418, 2386

Mittal R., et al., 2012, MNRAS, 426, 2957

Negri A., Posacki S., Pellegrini S., Ciotti L., 2014, MNRAS, 445, 1351

O'Sullivan E., Worrall D. M., Birkinshaw M., Trinchieri G., Wolter A., Zezas A., Giacintucci S., 2011, MNRAS, 416, 2916

Oonk J. B. R., Jaffe W., Bremer M. N., van Weeren R. J., 2010, MNRAS, 405, 898

Oosterloo T. A., Morganti R., Sadler E. M., van der Hulst T., Serra P., 2007, A&A, 465, 787

Paggi A., Fabbiano G., Kim D.-W., Pellegrini S., Civano F., Strader J., Luo B., 2014, ApJ, 787, 134

Phillips M. M., Jenkins C. R., Dopita M. A., Sadler E. M., Binette L., 1986, AJ, 91, 1062
Plana H., Boulesteix J., Amram P., Carignan C., Mendes de Oliveira C., 1998, A&AS, 128, 75
Prasad D., Sharma P., Babul A., 2015, ApJ, 811, 108
Pulido F. A., et al., 2018, ApJ, 853, 177
Randall S. W., et al., 2011, ApJ, 726, 86
Roncarelli M., et al., 2018, preprint, (arXiv:1805.02577)
Russell H. R., McNamara B. R., Edge A. C., Hogan M. T., Main R. A., Vantyghem A. N., 2013, MNRAS, 432, 530
Salomé P., Combes F., 2003, A&A, 412, 657
Sharma P., McCourt M., Quataert E., Parrish I. J., 2012, MNRAS, 420, 3174
Shin J., WenHao J.-H., Mulchaey J. S., 2016, ApJS, 227, 31
Smith E. P., Heckman T. M., 1989, ApJS, 69, 365
Soker N., 2016, New Astron. Rev., 75, 1
Sparks W. B., et al., 2012, ApJ, 750, L5
Sun M., 2012, New Journal of Physics, 14, 045004
Sun et al. 2018, in prep.
Temi P., Amblard A., Gitti M., Brighenti F., Gaspari M., Mathews W. G., David L., 2018, ApJ, 858, 17
Tremaine S., et al., 2002, ApJ, 574, 740
Trinchieri G., di Serego Alighieri S., 1991, AJ, 101, 1647
Valluri M., Anupama G. C., 1996, AJ, 112, 1390
Voit G. M., Donahue M., O'Shea B. W., Bryan G. L., Sun M., Werner N., 2015, ApJ, 803, L21
Voit G. M., Meece G., Li Y., O'Shea B. W., Bryan G. L., Donahue M., 2017, ApJ, 845, 80
Vollmer B., Reich W., Wielebinski R., 2004, A&A, 423, 57
Wang C., Li Y., Ruszkowski M., 2018, preprint, (arXiv:1805.03217)
Wenger M., et al., 2000, A&AS, 143, 9
Werner N., Durret F., Ohashi T., Schindler S., Wiersma R. P. C., 2008, Space Sci. Rev., 134, 337
Werner N., Allen S. W., Simionescu A., 2012, MNRAS, 425, 2731
Werner N., et al., 2013, ApJ, 767, 153
Werner N., et al., 2014, MNRAS, 439, 2291
Werner N., Lakhchaura K., Canning R. E. A., Gaspari M., Simionescu A., 2018, MNRAS,
Willingale R., Starling R. L. C., Beardmore A. P., Tanvir N. R., O'Brien P. T., 2013, MNRAS, 431, 394
Zhuravleva I., et al., 2014, Nature, 515, 85
de Vaucouleurs G., de Vaucouleurs A., Corwin Jr. H. G., Buta R. J., Paturel G., Fouqué P., 1991, Third Reference Catalogue of Bright Galaxies. Volume I: Explanations and references. Volume II: Data for galaxies between 0^h and 12^h. Volume III: Data for galaxies between 12^h and 24^h.

APPENDIX A:

Table A1. A log of the *Chandra* observations used in the paper.

Target Name	Obs ID	Instrument	Cleaned Exposure (ks)	Date of Observation
3C 449	11737	ACIS-S	45.29	2010-09-14
	13123	ACIS-S	51.73	2010-09-20
IC 1860	10537	ACIS-S	31.12	2009-09-12
IC 4296	2021	ACIS-S	14.20	2001-09-10
	3394	ACIS-S	16.22	2001-12-15
IC 4765	15637	ACIS-S	11.77	2013-03-29
NGC 57	10547	ACIS-S	8.89	2008-10-29
NGC 315	4156	ACIS-S	37.47	2003-02-22
NGC 410	5897	ACIS-S	2.05	2004-11-30
NGC 499	2882	ACIS-I	40.13	2002-01-08
	317	ACIS-S	19.17	2000-10-11
	10536	ACIS-S	17.62	2009-02-12
	10866	ACIS-S	8.05	2009-02-05
	10867	ACIS-S	6.04	2009-02-07
NGC 507	2882	ACIS-I	40.13	2002-01-08
	317	ACIS-S	19.17	2000-10-11
NGC 533	2880	ACIS-S	29.16	2002-07-28
NGC 708	7921	ACIS-S	105.53	2006-11-20
	2215	ACIS-S	26.45	2001-08-03
NGC 741	17198	ACIS-S	70.94	2015-12-04
	18718	ACIS-S	48.36	2015-12-06
	2223	ACIS-S	24.20	2001-01-28
NGC 777	5001	ACIS-I	7.67	2004-12-23
NGC 1132	801	ACIS-S	10.92	1999-12-10
	3576	ACIS-S	28.16	2003-11-16
NGC 1316	2022	ACIS-S	23.55	2001-04-17
NGC 1399	14529	ACIS-S	29.31	2015-11-06
	16639	ACIS-S	27.38	2014-10-12
NGC 1404	17549	ACIS-S	60.63	2015-03-28
	2942	ACIS-S	25.66	2003-02-13
	16231	ACIS-S	53.58	2014-10-20
	17540	ACIS-S	25.98	2014-11-02
	17541	ACIS-S	19.61	2014-10-23
	16232	ACIS-S	57.89	2014-11-12
	16233	ACIS-S	83.41	2014-11-09
	17548	ACIS-S	40.29	2014-11-11
	16234	ACIS-S	78.30	2014-10-30
NGC 1407	14033	ACIS-S	45.29	2012-06-17
	791	ACIS-S	38.85	2000-08-16
NGC 1521	10539	ACIS-S	43.51	2009-07-04
NGC 1550	3186	ACIS-I	9.22	2002-01-08
	3187	ACIS-I	9.13	2002-01-08
NGC 1600	4283	ACIS-S	20.90	2002-09-18
	4371	ACIS-S	19.07	2002-09-20
NGC 2300	4968	ACIS-S	37.12	2004-06-23
	15648	ACIS-S	15.53	2013-05-24
NGC 2305	10549	ACIS-S	8.64	2009-07-19
NGC 3091	3215	ACIS-S	22.51	2002-03-26
NGC 3923	1563	ACIS-S	16.24	2001-06-14
	9507	ACIS-S	65.37	2008-04-11
NGC 4073	3234	ACIS-S	26.10	2002-11-24
NGC 4125	2071	ACIS-S	47.34	2001-09-09
NGC 4261	9569	ACIS-S	87.63	2008-02-12
	834	ACIS-S	17.92	2000-05-06
NGC 4374	803	ACIS-S	25.91	2000-05-19
	401	ACIS-S	1.25	2000-04-20
NGC 4406	318	ACIS-S	13.31	2000-04-07
	16967	ACIS-I	19.04	2016-05-02
NGC 4472	15757	ACIS-I	25.07	2014-04-18
	12888	ACIS-S	139.77	2011-02-21
	12889	ACIS-S	116.73	2011-02-14
	321	ACIS-S	32.25	2000-06-12
	322	ACIS-I	8.57	2000-03-19
NGC 4486	241	ACIS-S	36.76	2000-07-17
	2707	ACIS-S	98.69	2000-07-17
	352	ACIS-S	37.68	2000-07-29
	5826	ACIS-I	126.76	2005-03-03
	5827	ACIS-I	156.20	2005-05-05
	6186	ACIS-I	51.55	2005-01-31
	7212	ACIS-I	65.23	2005-11-14

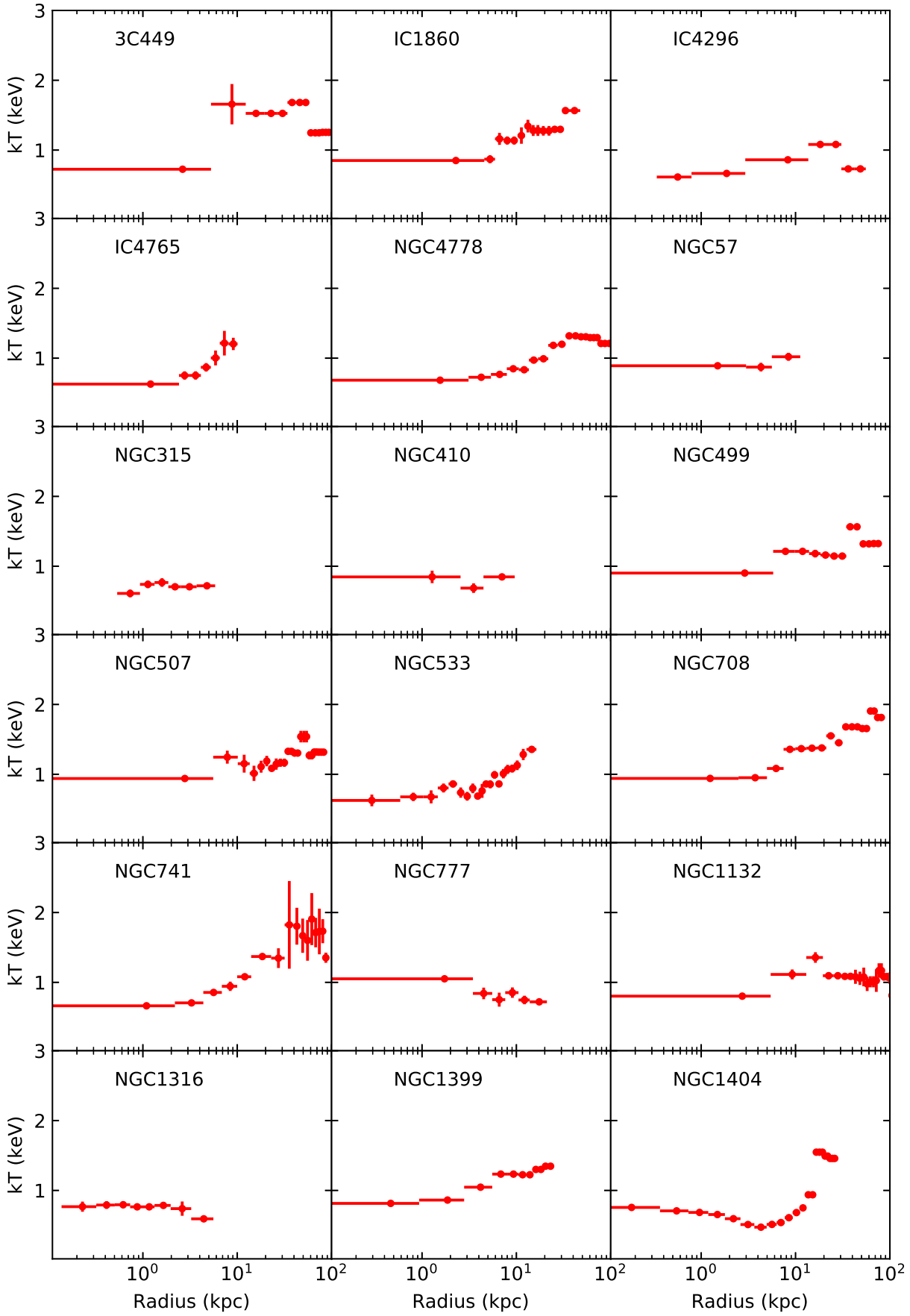

Figure A.1. Deprojected temperature profiles of the individual galaxies.

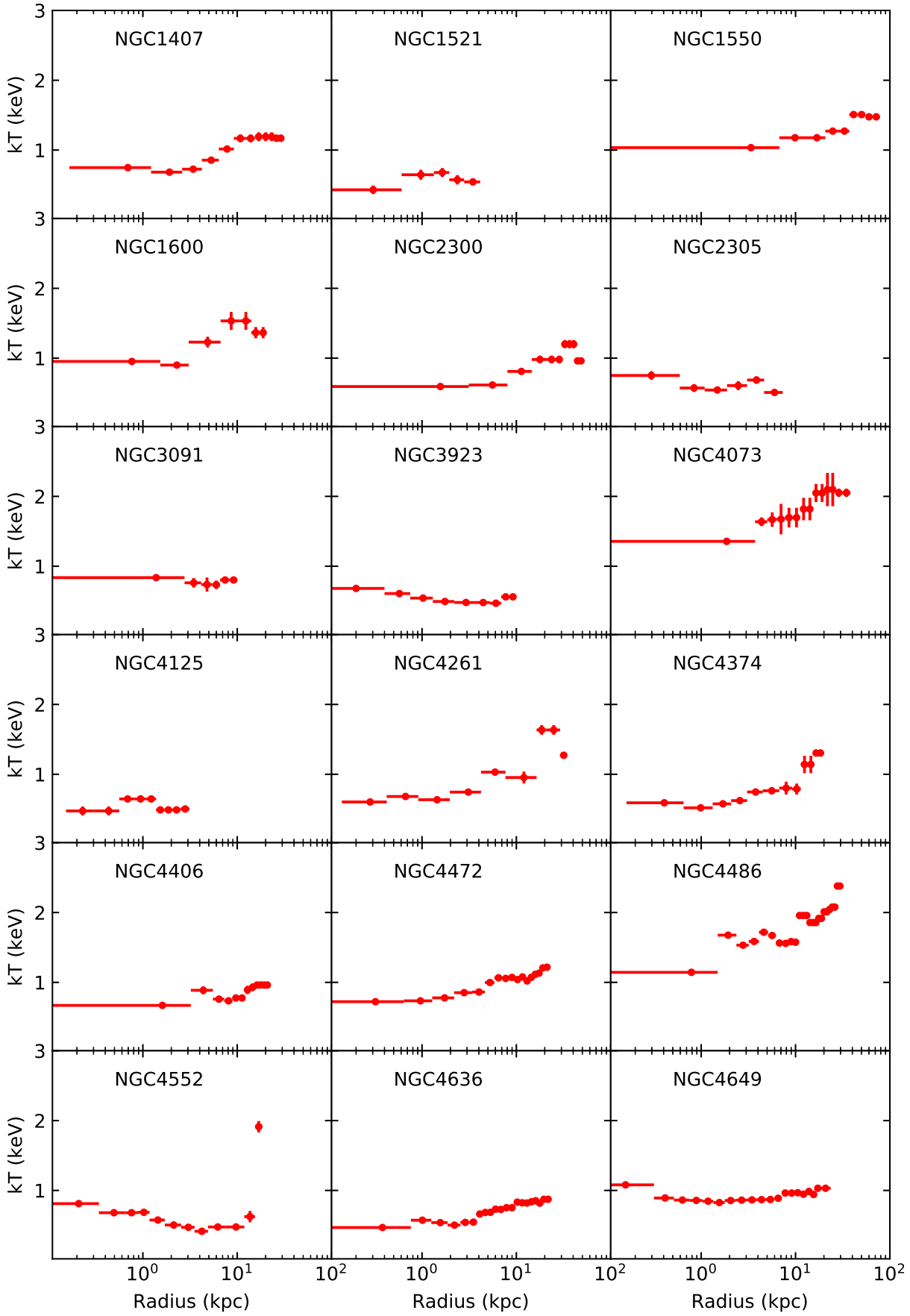

Figure A.1. Deprojected temperature profiles of the individual galaxies (continued).

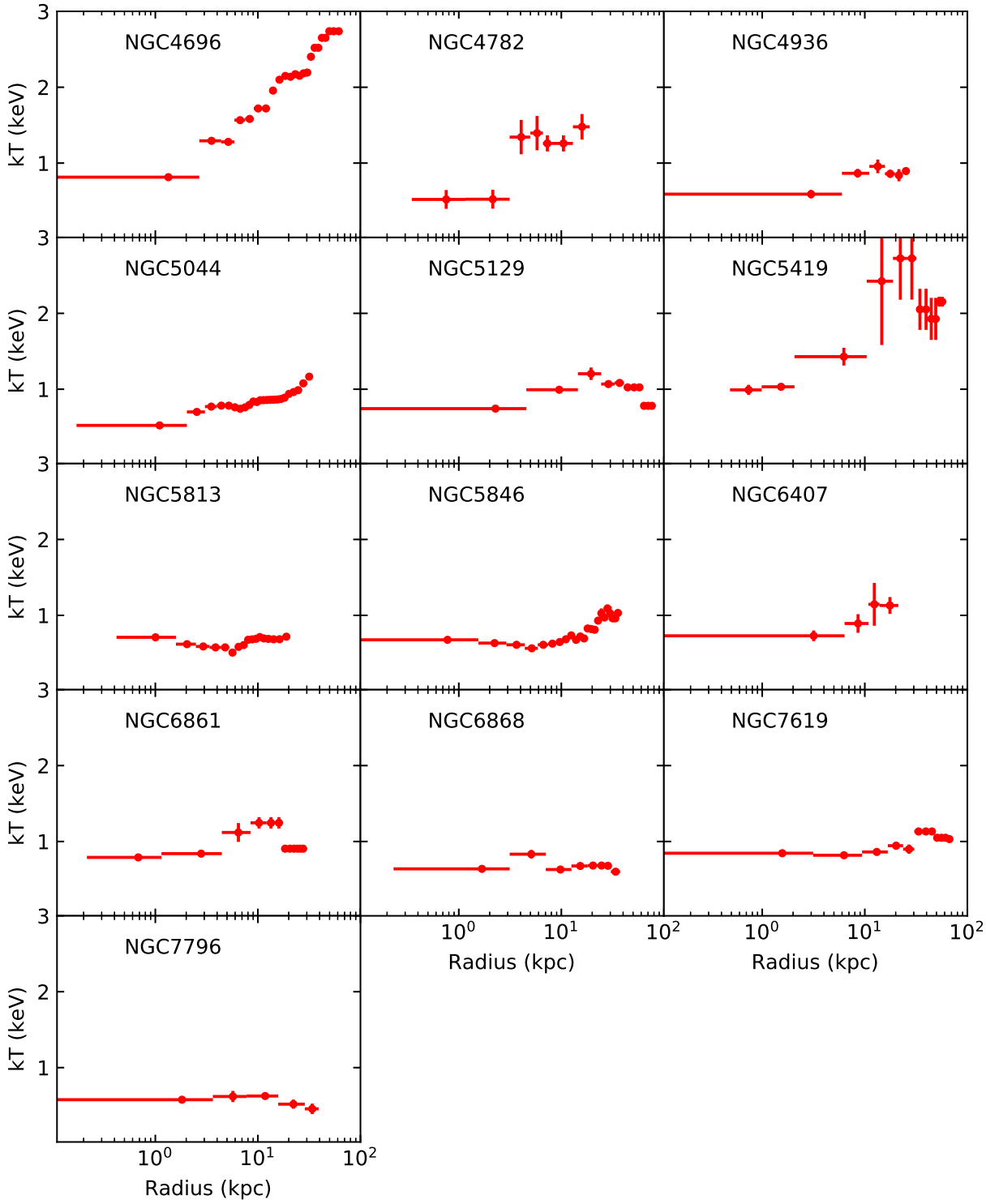

Figure A.1. Deprojected temperature profiles of the individual galaxies (continued).

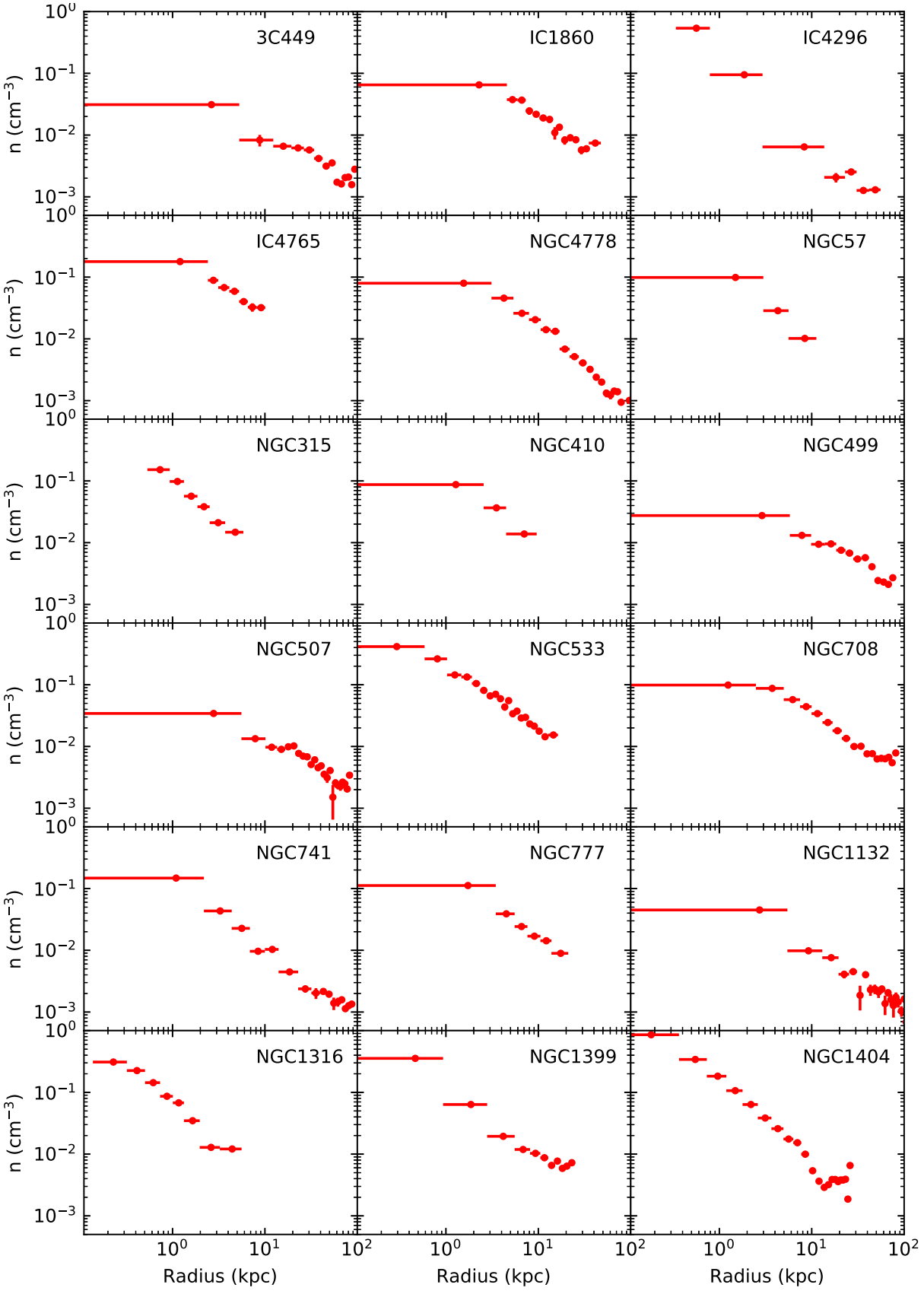

Figure A.2. Deprojected density profiles of the individual galaxies.

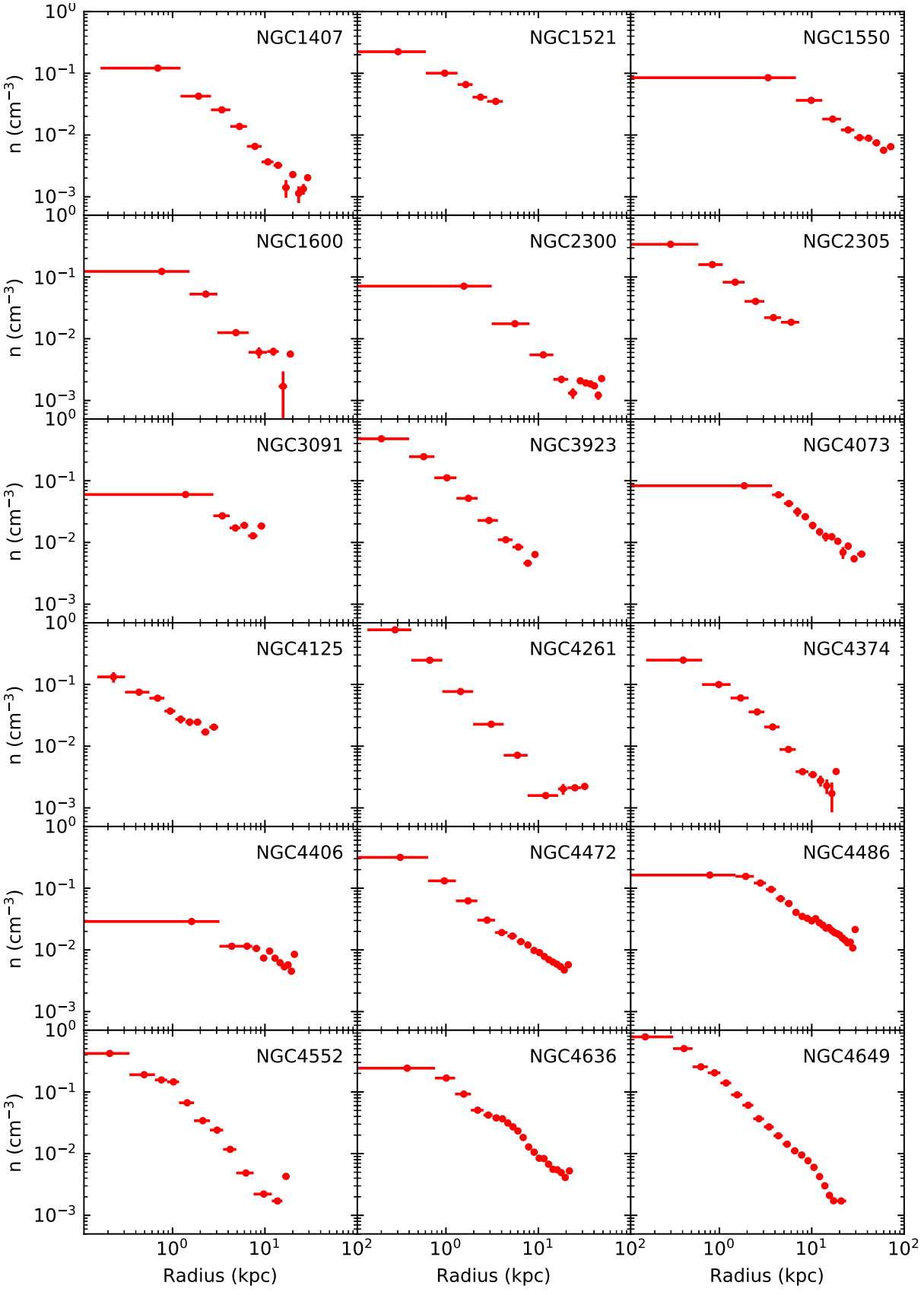

Figure A.2. Deprojected density profiles of the individual galaxies (continued).

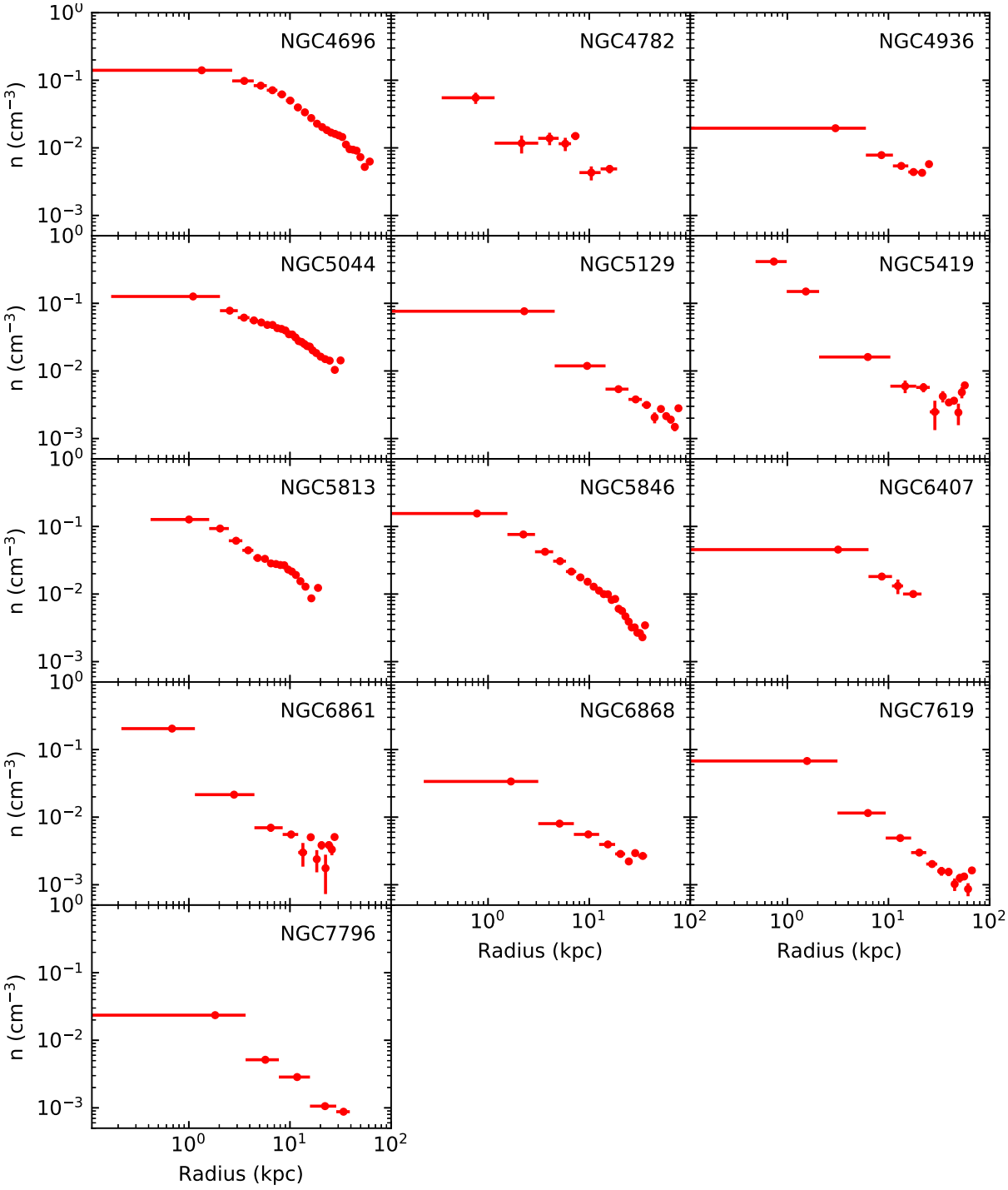

Figure A.2. Deprojected density profiles of the individual galaxies (continued).

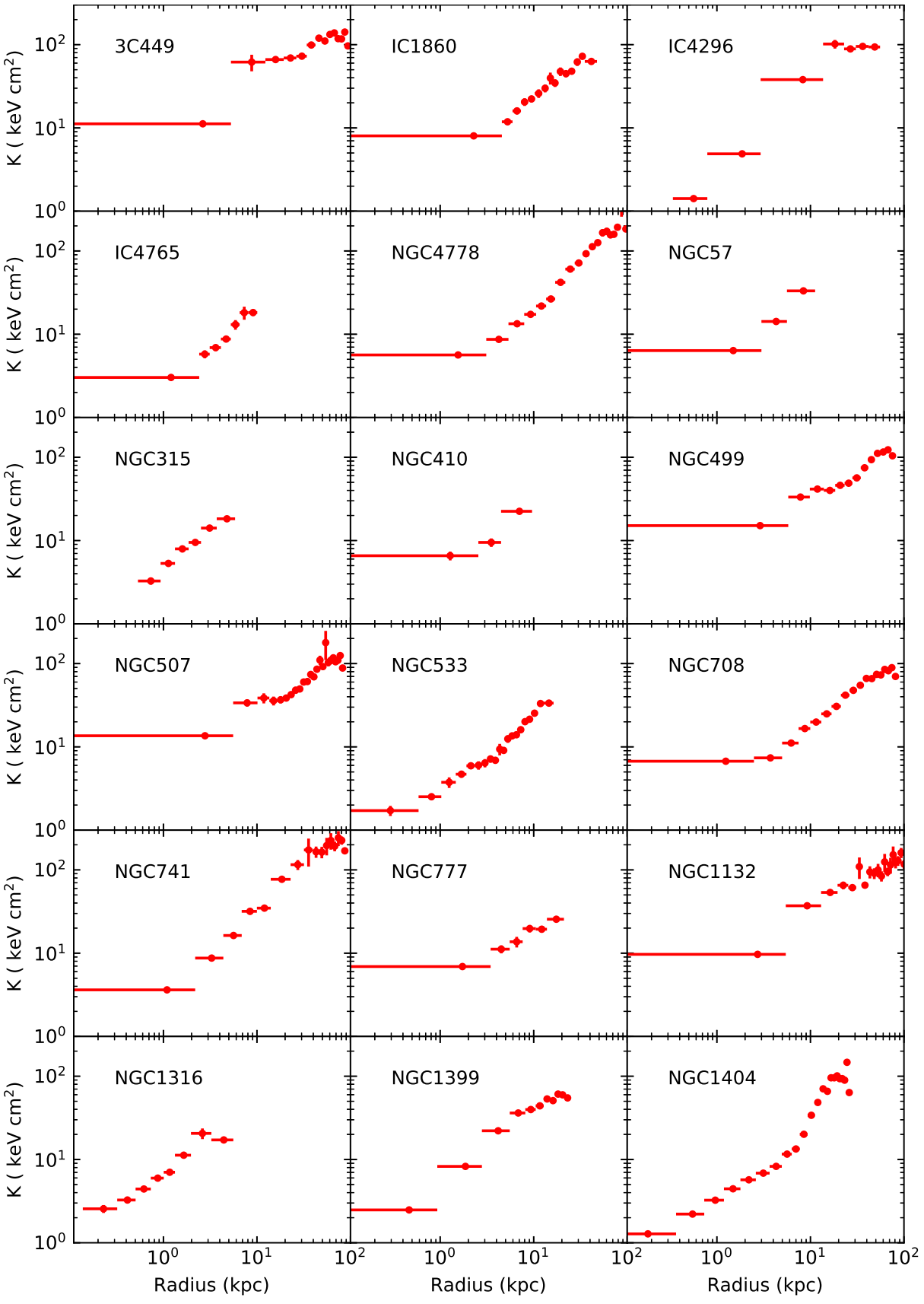

Figure A.3. Deprojected entropy profiles of the individual galaxies.

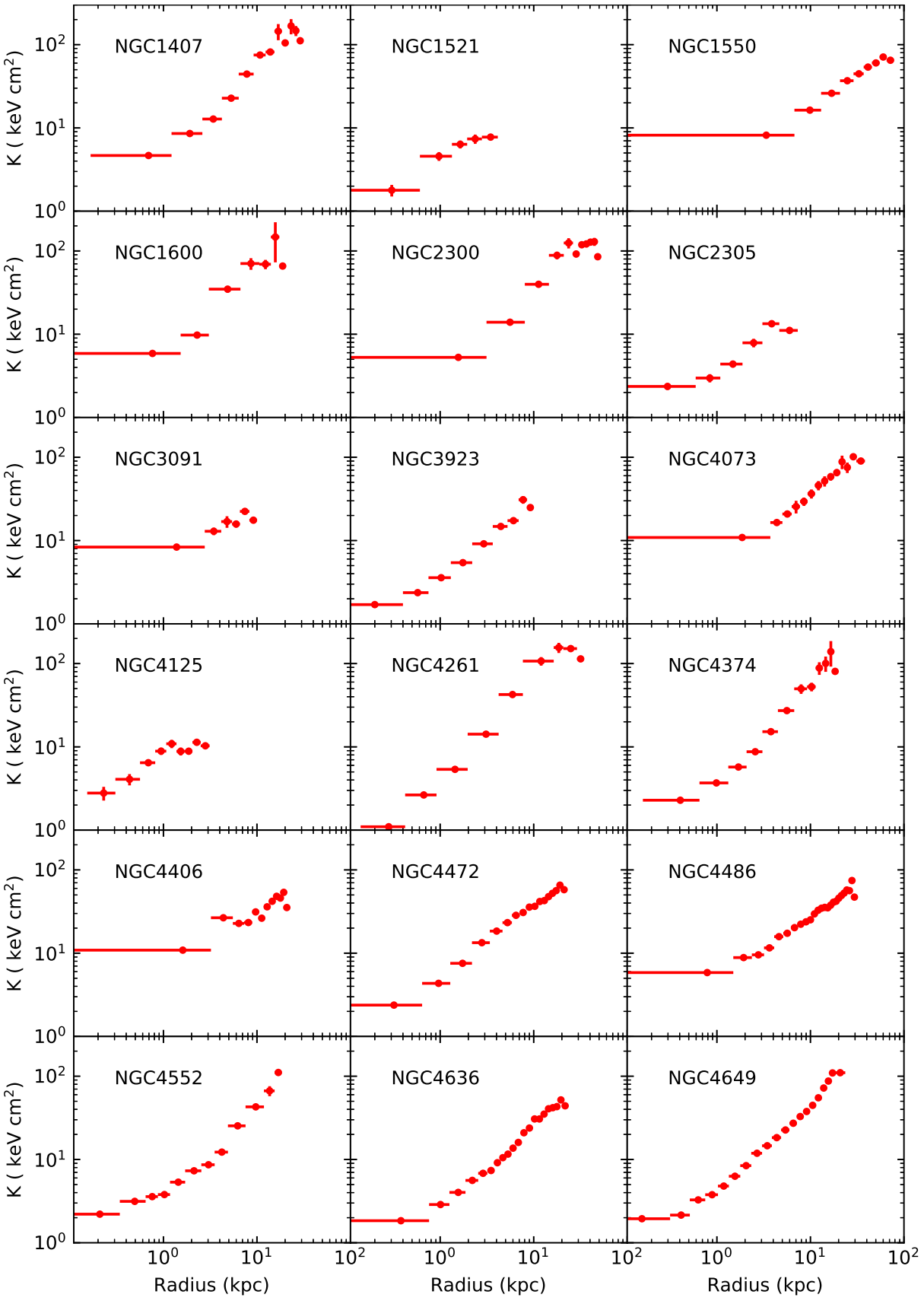

Figure A.3. Deprojected entropy profiles of the individual galaxies (continued).

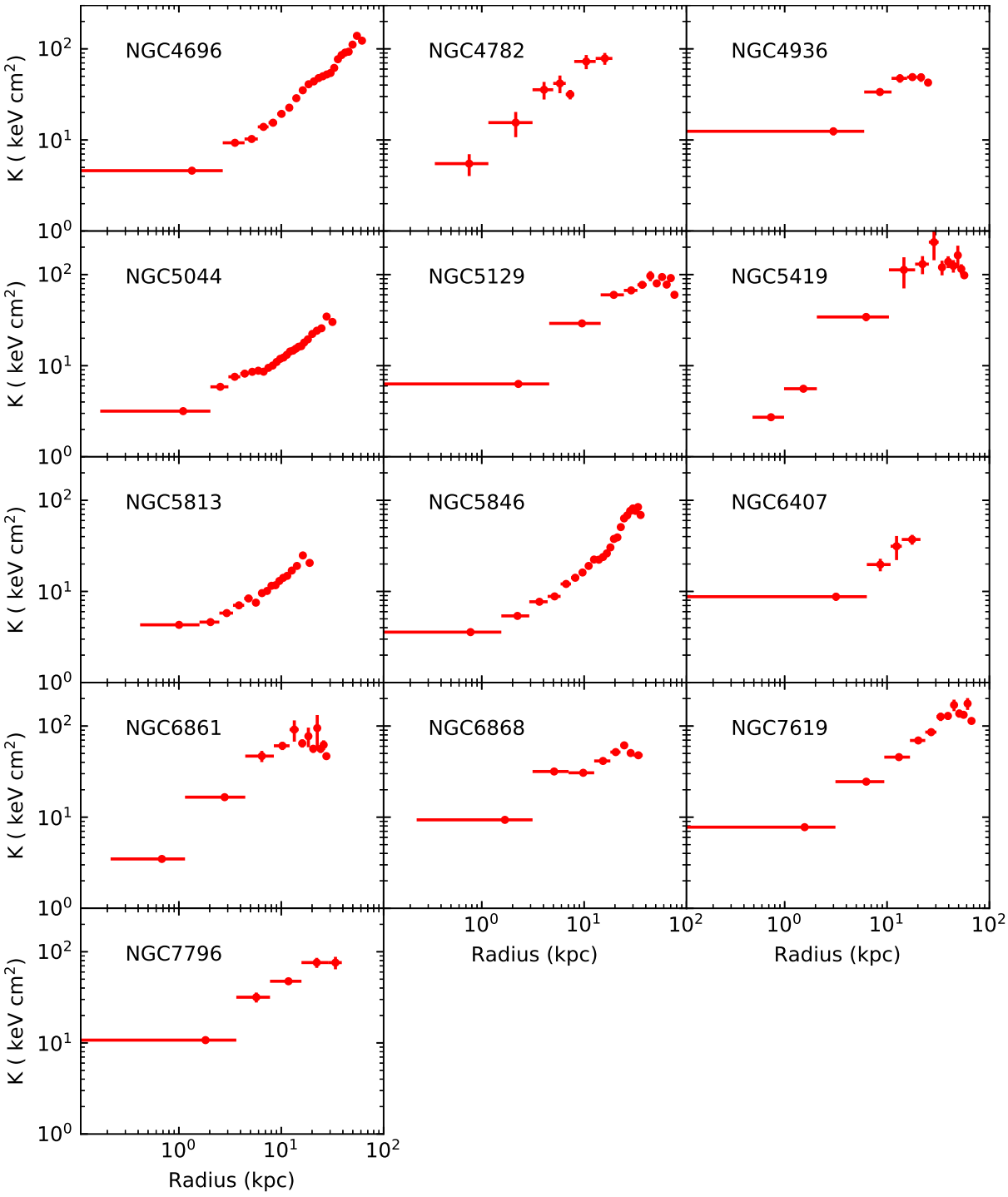

Figure A.3. Deprojected entropy profiles of the individual galaxies (continued).

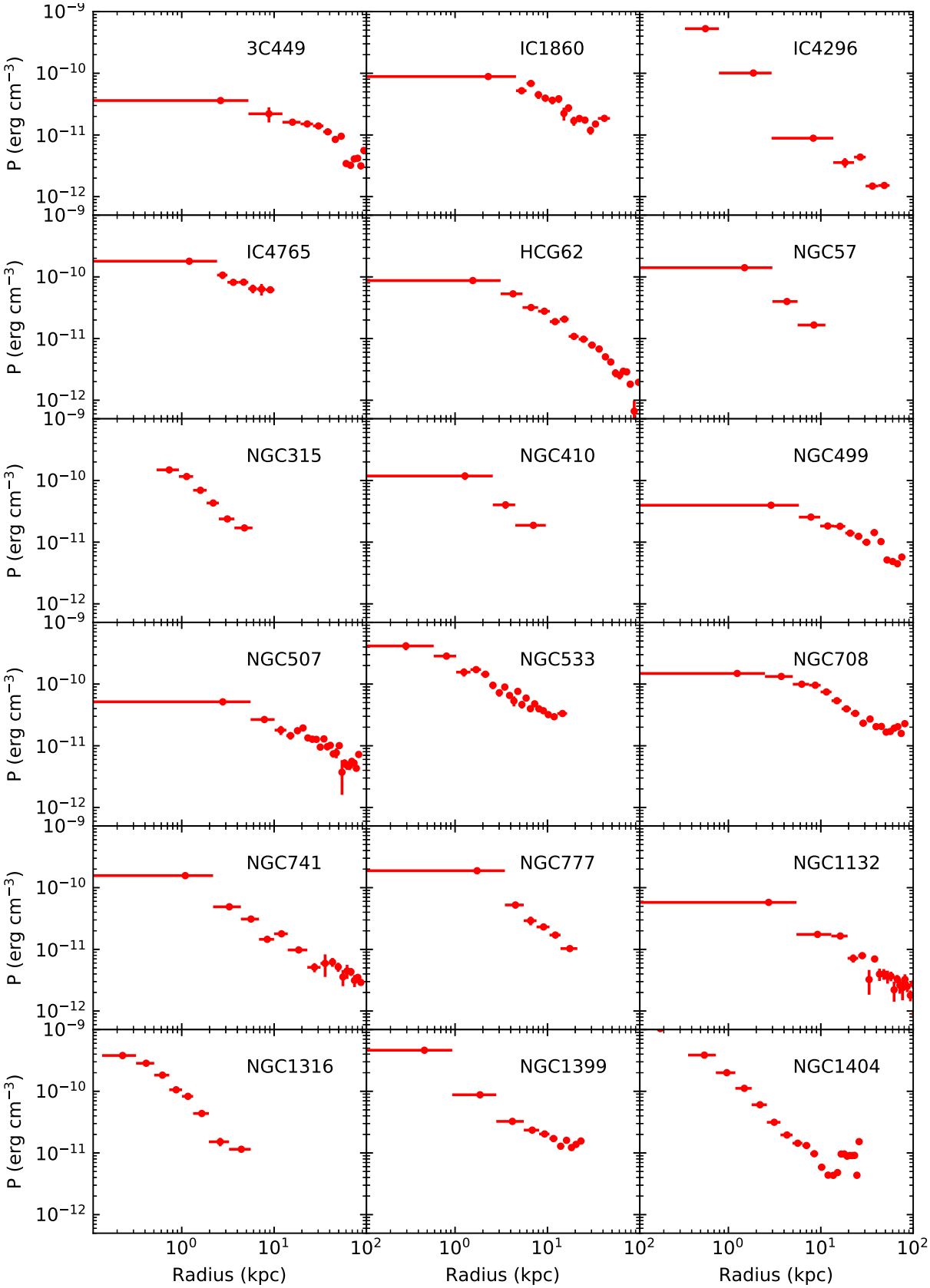

Figure A.4. Deprojected pressure profiles of the individual galaxies.

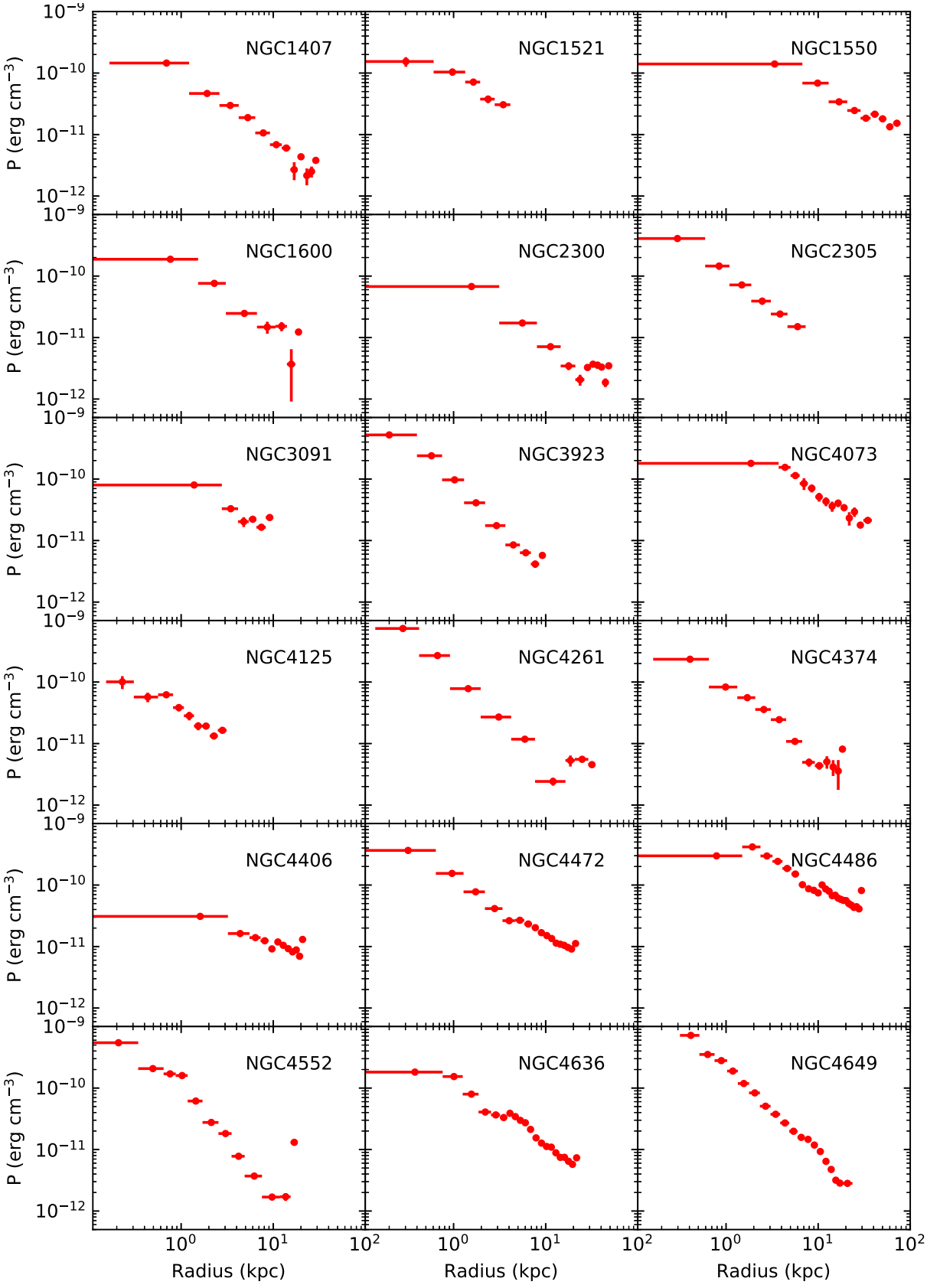

Figure A.4. Deprojected pressure profiles of the individual galaxies (continued).

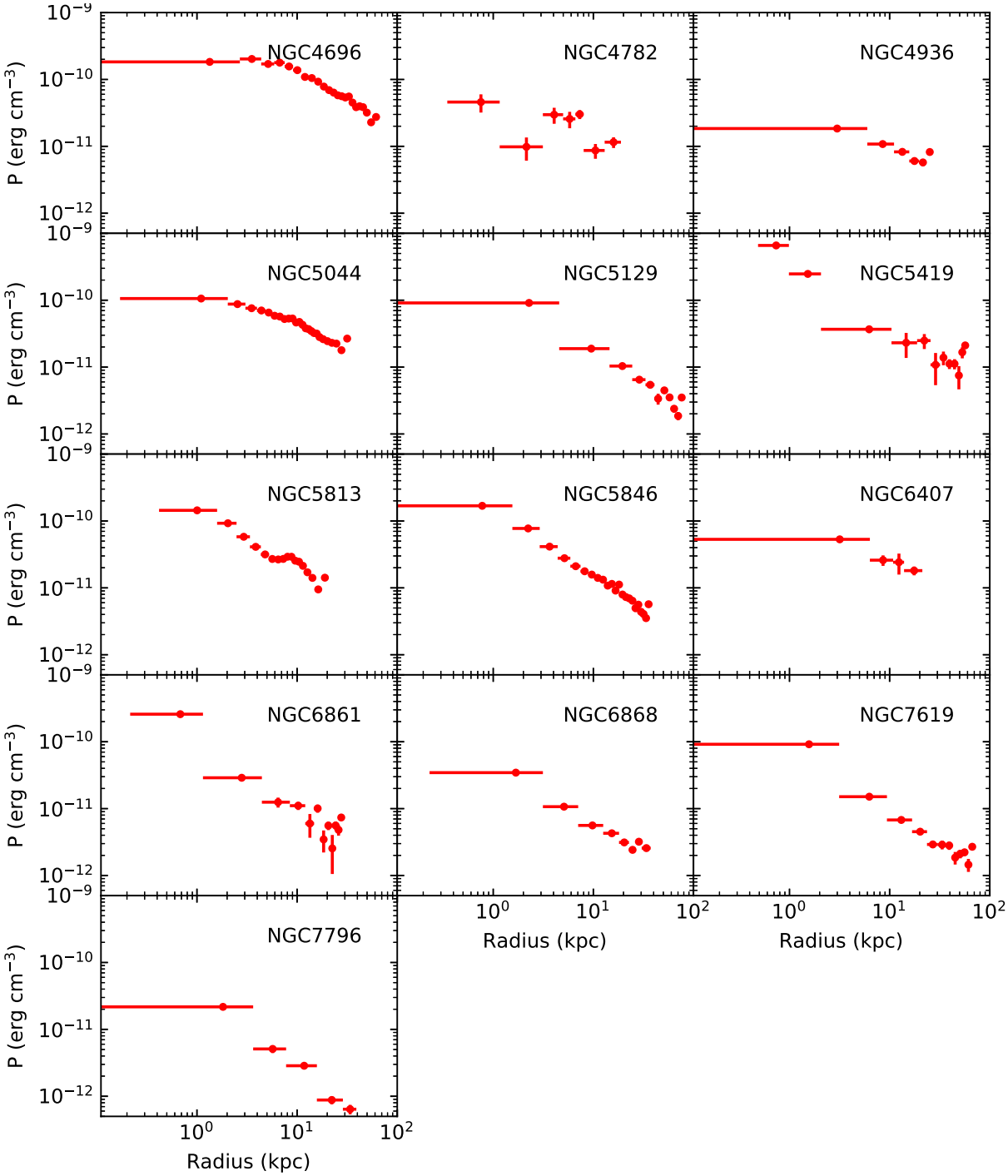

Figure A.4. Deprojected pressure profiles of the individual galaxies (continued).

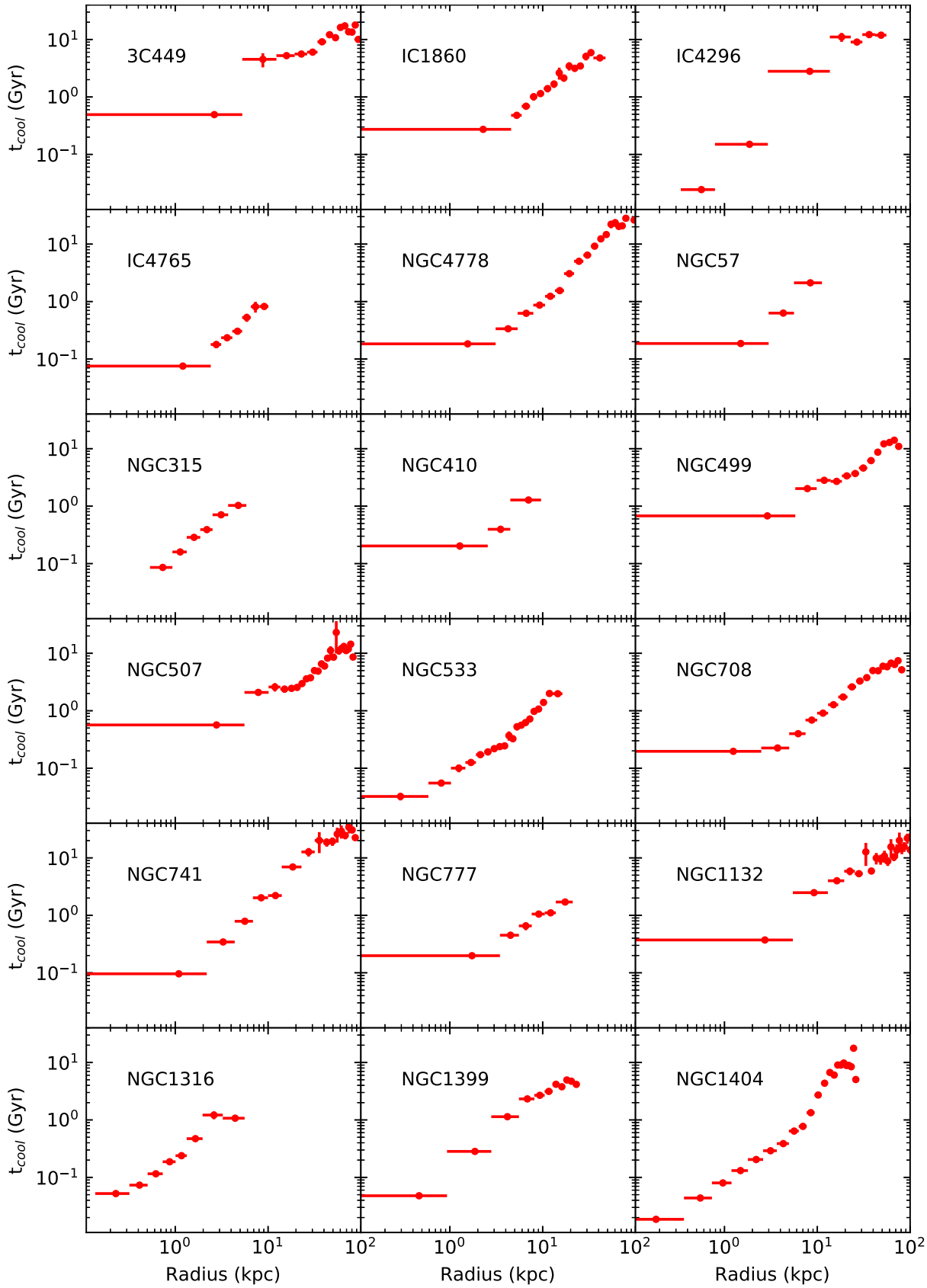

Figure A.5. Cooling time profiles of the individual galaxies.

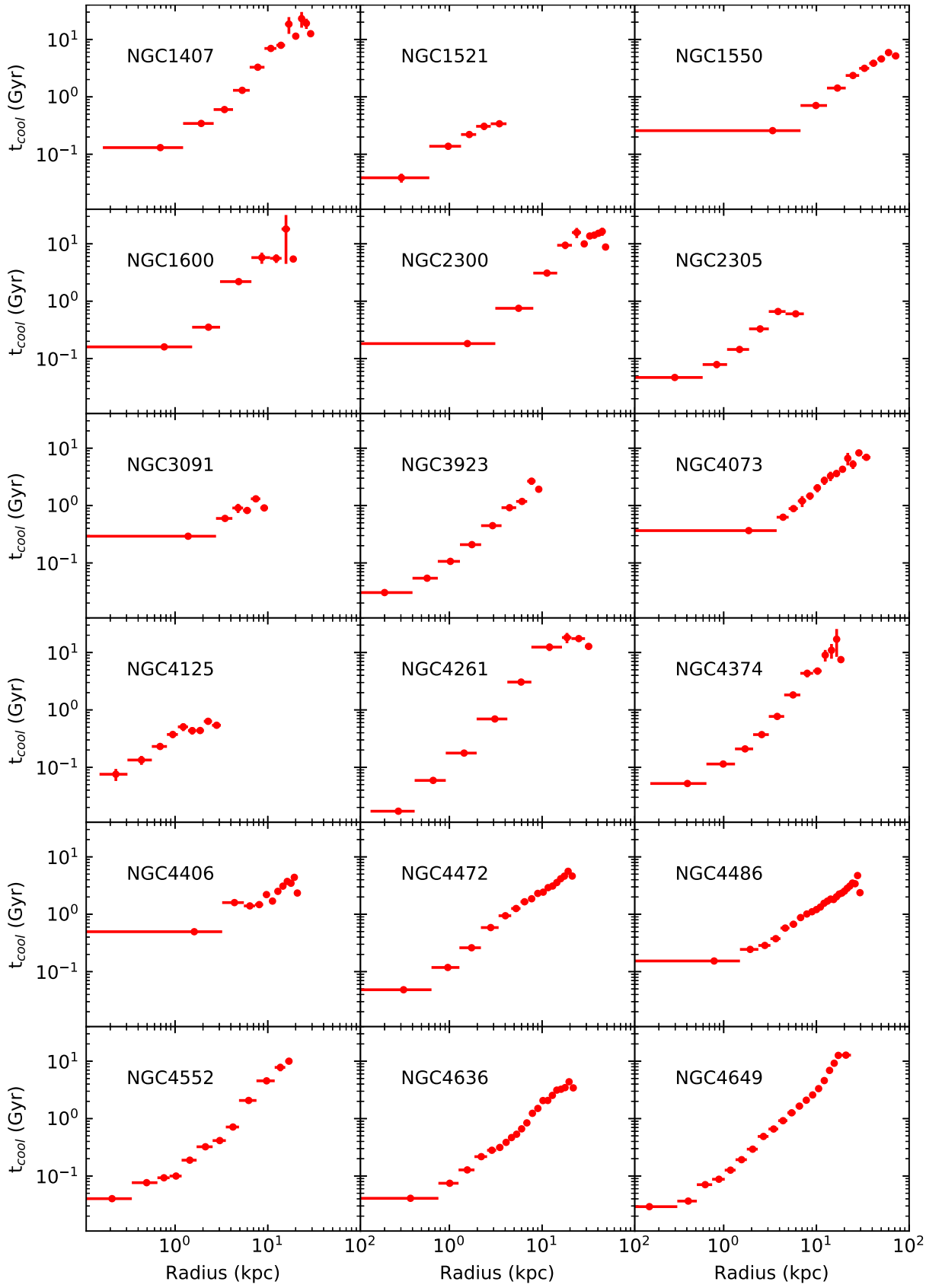

Figure A.5. Cooling time profiles of the individual galaxies (continued).

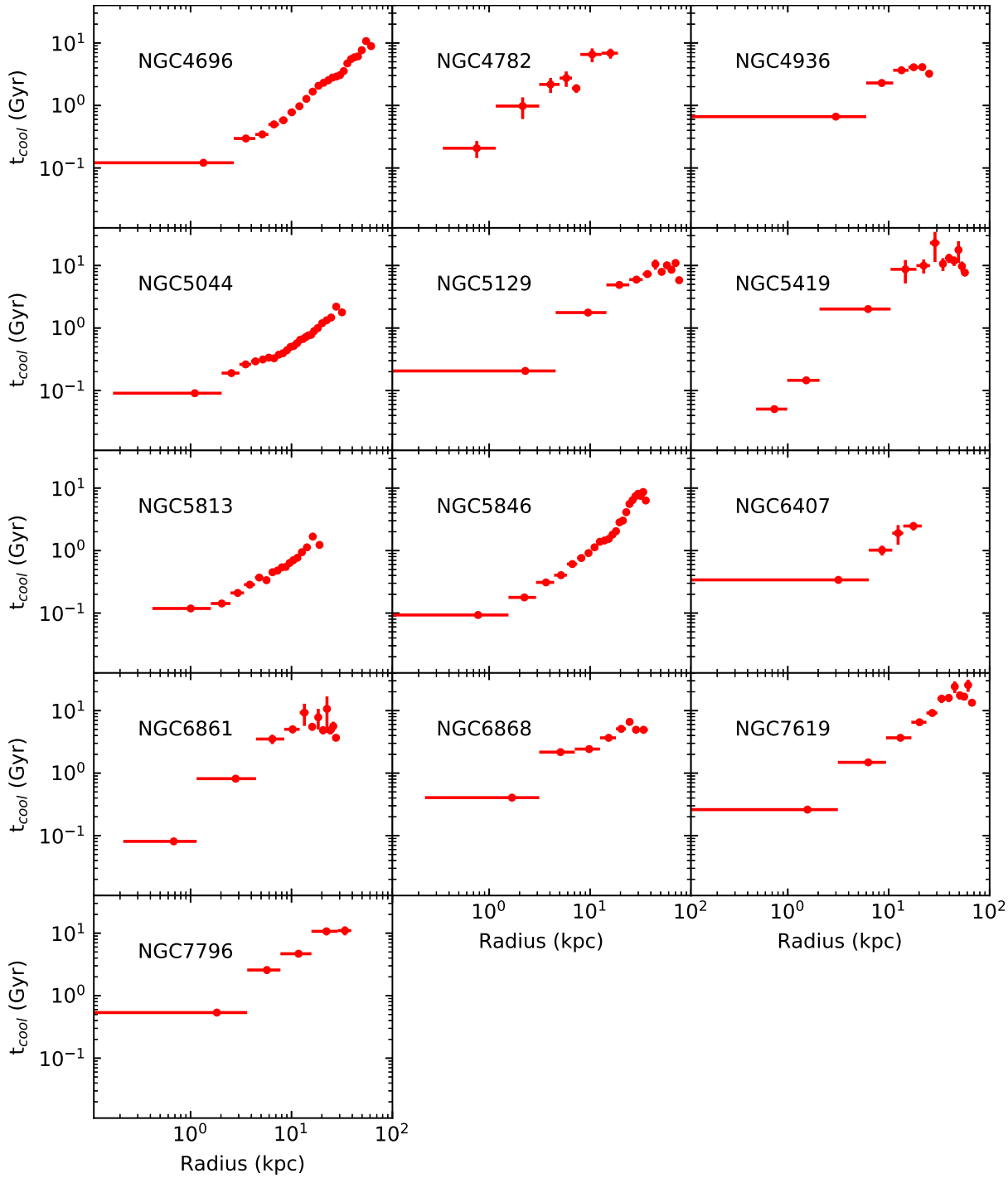

Figure A.5. Cooling time profiles of the individual galaxies (continued).

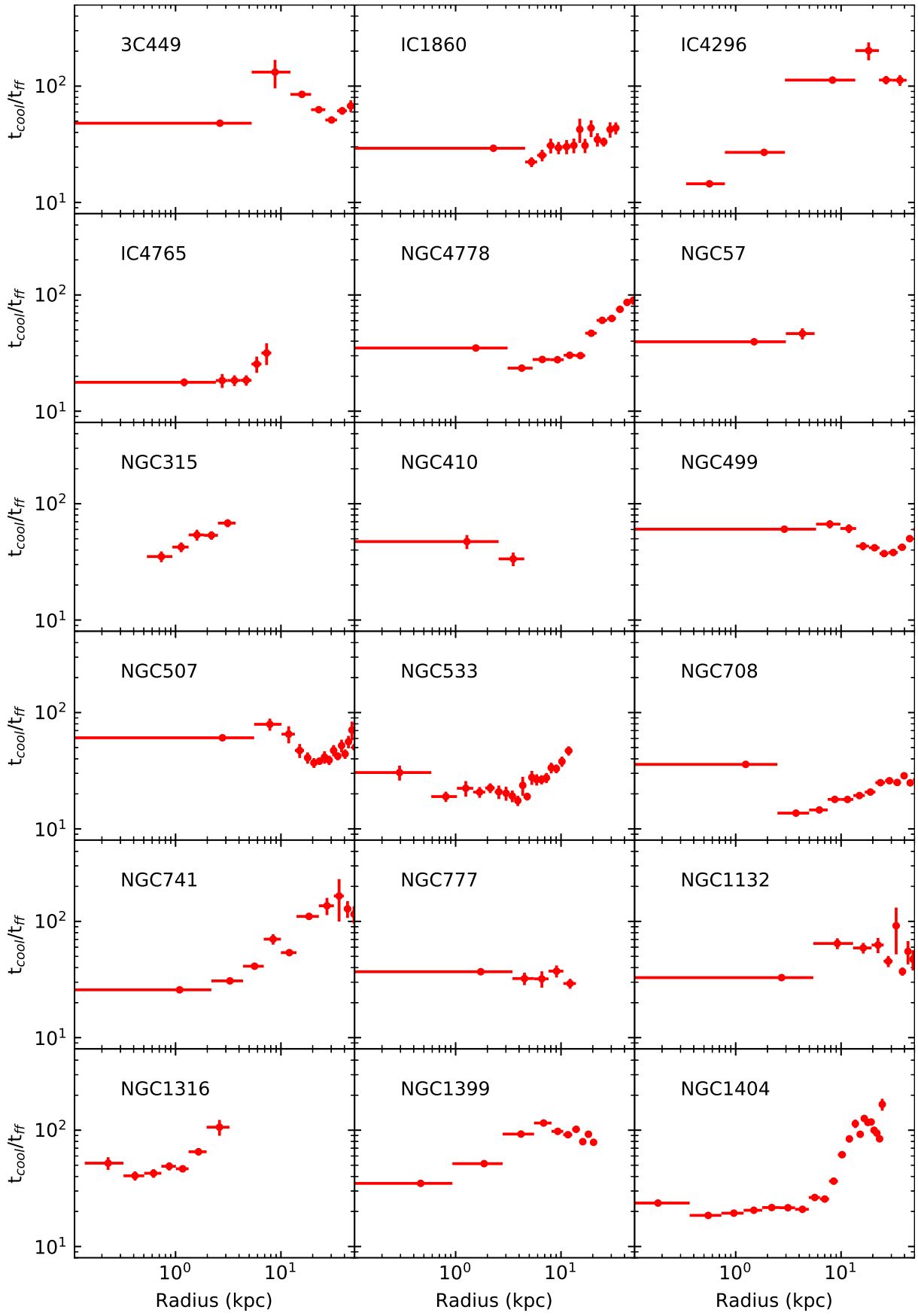

Figure A.6. $t_{\rm cool}/t_{\rm ff}$ profiles of the individual galaxies.

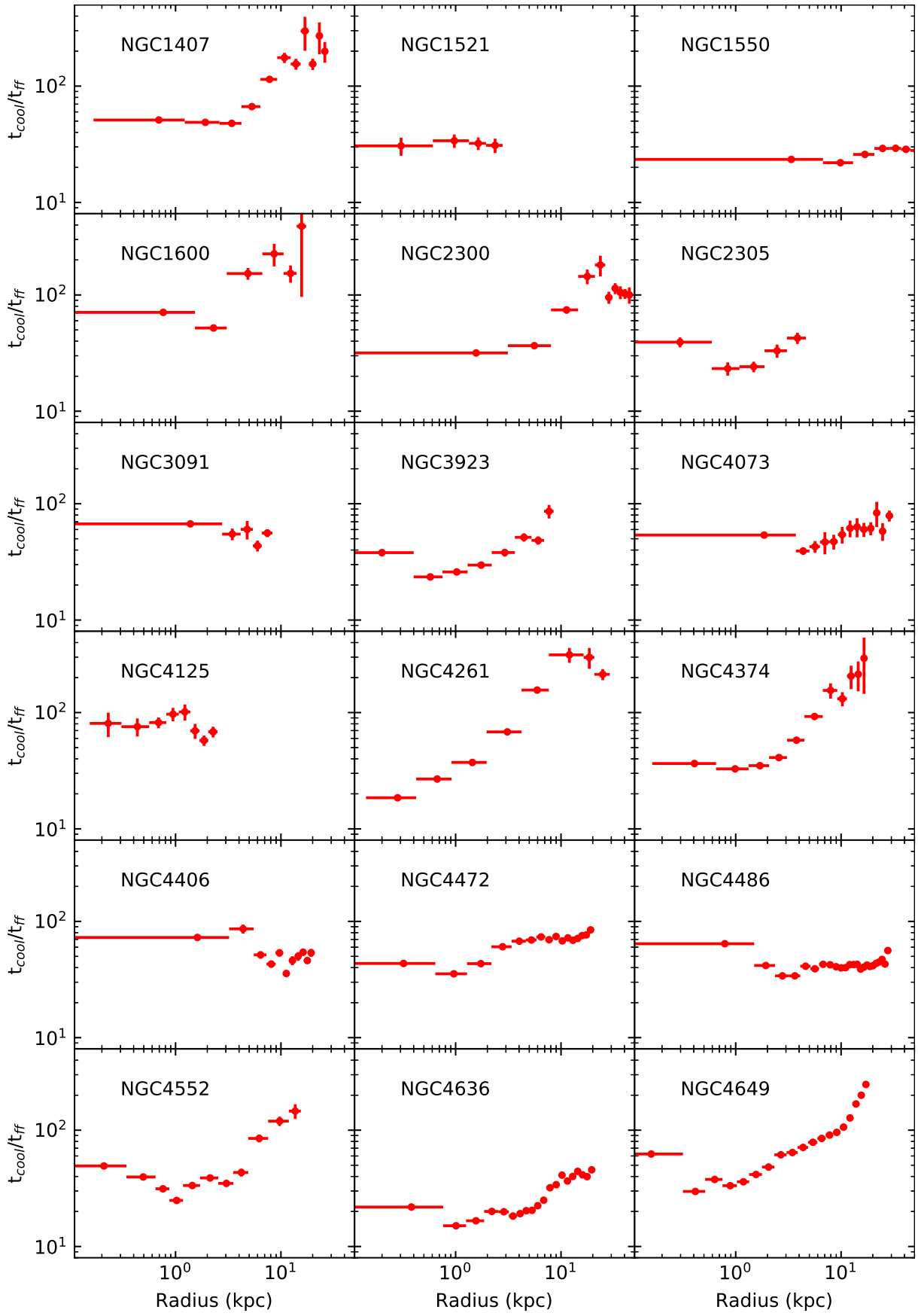

Figure A.6. $t_{\rm cool}/t_{\rm ff}$ profiles of the individual galaxies (continued).

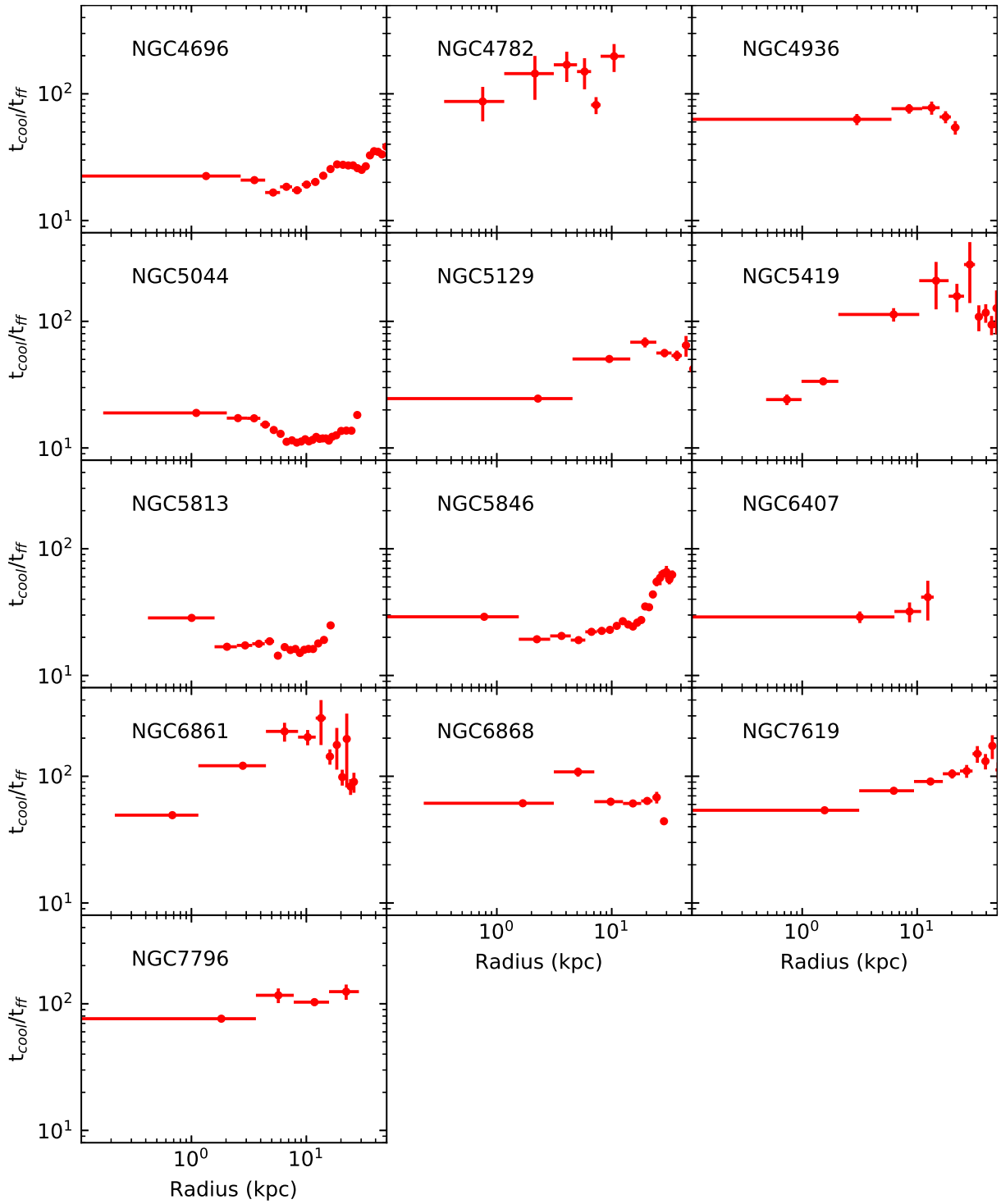

Figure A.6. $t_{\rm cool}/t_{\rm ff}$ profiles of the individual galaxies (continued).

Table A1. A log of the *Chandra* observations used in the paper (Continued).

Target Name	Obs ID	Instrument	Cleaned Exposure (ks)	Date of Observation
NGC 4552	14359	ACIS-S	44.01	2012-04-23
	14358	ACIS-S	41.45	2012-08-10
	2072	ACIS-S	44.01	2001-04-22
	13985	ACIS-S	41.19	2012-04-22
NGC 4636	323	ACIS-S	48.80	2000-01-26
	324	ACIS-I	3.17	1999-12-04
	3926	ACIS-I	65.24	2003-02-14
	4415	ACIS-I	66.43	2003-02-15
NGC 4649	8182	ACIS-S	39.83	2007-01-30
	8507	ACIS-S	14.96	2007-02-01
	12975	ACIS-S	73.44	2011-08-08
	14328	ACIS-S	11.92	2011-08-12
	12976	ACIS-S	86.94	2011-02-24
	785	ACIS-S	33.02	2000-04-20
NGC 4696	1560	ACIS-S	45.56	2001-04-18
	16223	ACIS-S	175.38	2014-05-26
	16224	ACIS-S	40.76	2014-04-09
	16225	ACIS-S	29.33	2014-04-26
	16534	ACIS-S	54.68	2014-06-05
	16607	ACIS-S	44.78	2014-04-12
	16608	ACIS-S	33.35	2014-04-07
	16609	ACIS-S	80.54	2014-05-04
	16610	ACIS-S	16.57	2014-04-27
	4190	ACIS-S	34.00	2003-04-18
	4191	ACIS-S	32.74	2003-04-18
	4954	ACIS-S	87.26	2004-04-01
	4955	ACIS-S	44.68	2004-04-02
	504	ACIS-S	31.48	2000-05-22
	505	ACIS-S	9.96	2000-06-08
	5310	ACIS-S	48.56	2004-04-04
NGC 4778	2230	ACIS-I	8.70	2001-01-08
	10462	ACIS-S	57.57	2009-03-02
	10874	ACIS-S	47.59	2009-03-03
	921	ACIS-S	40.44	2000-01-25
NGC 4782	3220	ACIS-S	39.16	2002-06-16
NGC 4936	4997	ACIS-I	10.23	2004-02-09
	4998	ACIS-I	12.54	2004-02-15
NGC 5044	798	ACIS-S	17.91	2000-03-19
	9399	ACIS-S	73.68	2008-03-07
	17195	ACIS-S	66.51	2015-06-06
	17196	ACIS-S	75.04	2015-05-11
	17653	ACIS-S	30.16	2015-05-07
	17654	ACIS-S	21.21	2015-05-10
	17666	ACIS-S	73.95	2015-08-23
	3225	ACIS-S	63.40	2002-06-07
	3664	ACIS-S	47.76	2002-06-06
NGC 5129	7325	ACIS-S	21.74	2006-05-14
	6944	ACIS-S	17.07	2006-04-13
NGC 5419	5000	ACIS-I	12.51	2004-06-19
	4999	ACIS-I	14.58	2004-06-18
NGC5813	9517	ACIS-S	88.25	2008-06-05
	12951	ACIS-S	62.21	2011-03-28
	12952	ACIS-S	114.64	2011-04-05
	12953	ACIS-S	26.62	2011-04-07
	13246	ACIS-S	36.31	2011-03-30
	13247	ACIS-S	30.64	2011-03-31
	13253	ACIS-S	92.92	2011-04-08
	13255	ACIS-S	35.72	2011-04-10
	5907	ACIS-S	36.85	2005-04-02
NGC 5846	7923	ACIS-I	79.01	2007-06-12
	788	ACIS-S	17.58	2000-05-24
NGC 6407	5896	ACIS-S	1.90	2005-05-24
NGC 6861	11752	ACIS-I	83.01	2009-08-13
NGC 6868	3191	ACIS-I	20.65	2002-11-01
	11753	ACIS-I	63.90	2009-08-19
NGC 7619	3955	ACIS-S	30.31	2003-09-24
	2074	ACIS-I	22.14	2001-08-20
NGC 7796	7061	ACIS-S	44.51	2006-08-28
	7401	ACIS-S	17.65	2006-09-03